



Progress of Experimental Studies in the HL-2A Tokamak

M. Xu¹ · X. R. Duan¹ · Yi Liu¹ · W. L. Zhong¹ · M. Jiang¹ · G. L. Xiao¹ · P. W. Shi¹ · T. Long¹ · X. Y. Bai¹ · Y. Shen¹ · Z. Y. Cui¹ · D. L. Yu¹ · Y. P. Zhang¹ · W. Chen¹ · L. M. Yu¹ · R. Hong¹ · B. D. Yuan¹ · J. B. Yuan¹ · A. S. Liang¹ · T. F. Sun¹ · Y. Q. Liu¹ · L. W. Yan¹ · D. Q. Liu¹ · Z. Cao¹ · L. J. Cai¹ · Y. Q. Wang¹ · H. J. Li¹ · B. Lu¹ · H. L. Wei¹ · J. Y. Cao¹ · M. Huang¹ · Q. W. Yang¹ · Z. B. Shi¹ · G. Y. Zheng¹ · J. H. Zhang¹ · X. Q. Ji¹ · J. Q. Li¹ · G. Z. Hao¹ · X. M. Song¹ · W. M. Xuan¹ · X. T. Ding¹ · J. Q. Dong¹

Accepted: 7 January 2021 / Published online: 25 February 2021

© The Author(s), under exclusive licence to Springer Science+Business Media, LLC part of Springer Nature 2021

Abstract

During the last several years, the HL-2A experiment has made significant progress in the following areas: (1) lower-hybrid wave (LHW) heating and current drive, (2) plasma confinement and turbulent transport, (3) magnetohydrodynamic (MHD) instabilities and energetic particle physics and (4) H-mode and edge localized mode (ELM) control. The results show that the LHW system working in the co-current mode can reach higher driving efficiency and full non-inductive lower-hybrid current drive (LHCD) has been achieved. The intrinsic poloidal torque characterized by the divergence of the residual stress is deduced from synthesis for the first time. The dynamics of spectral symmetry breaking in drift wave turbulence is in good agreement with the development of the poloidal torque to drive the edge poloidal flow. The influence of the cross-phase dynamics on turbulent stress was also investigated. The ion internal transport barrier has been observed in the NBI-heated plasma, and inside the barrier the ion thermal transport is reduced to the neoclassical level. Besides, micro-turbulence is modulated by the rotation frequency of the magnetic island, and this modulation effect is related to a critical island width. Strong $E \times B$ shear is found at the island boundary. Three kinds of axisymmetric modes, beta-induced Alfvén eigenmode (BAE), toroidal Alfvén eigenmode (TAE) and the ellipticity-induced Alfvén eigenmode (EAE), are found to be driven unstable by nonlinear mode coupling between Alfvén eigenmodes and tearing mode which is well explained by the nonlinear gyrokinetic theory. The fishbone and tearing modes were actively controlled by the electron cyclotron resonance heating (ECRH). The dynamics of the edge plasma flows and turbulence during the L–I–H transition have been dedicatedly investigated. The geodesic acoustic mode (GAM) and limit cycle oscillation (LCO) coexist for a short time and disappear in the H-mode plasma with the increasing of $E \times B$ shear flow before the I–H transition, which plays an important role in the turbulence suppression. Different techniques, such as LHW, ECRH, resonant magnetic perturbation (RMP), and impurity seeding by the laser blow-off (LBO) and supersonic molecular beam injection (SMBI), have been successfully applied to control the large ELMs. It has been found that pedestal turbulence enhancement might be responsible for the observed mitigation effect.

Keywords HL-2A · Plasma confinement and turbulent transport · MHD · Energetic particle · H-mode · Edge localized mode

Introduction

The central theme of the HL-2A research program is to explore the key physics related to ITER and the advanced operation of tokamaks, such as the heating and current drive physics, access of H-mode, edge-localized mode (ELM) mitigation/suppression, core/edge turbulent transport and energetic particle physics. The HL-2A tokamak

✉ W. L. Zhong
zhongwl@swip.ac.cn

X. R. Duan
duanxr@swip.ac.cn

¹ Southwestern Institute of Physics,
PO Box 432, Chengdu 610041, China

[1] is a medium-sized tokamak with the major radius $R_0 = 1.65$ m and the minor radius $a \approx 0.4$ m. The main plasma parameters are: plasma current $I_p = 150\text{--}430$ kA, the toroidal magnetic field $B_t = 1.3\text{--}2.7$ T, the central line-averaged density $\bar{n}_e = (1 - 6) \times 10^{19} \text{ m}^{-3}$, and the central electron and ion temperatures are 5 keV and 3.5 keV, respectively.

The auxiliary heating has been promoted since 2016. The total neutral beam injection (NBI) power exceeds 1.2 MW, with a single beam source achieving 15 A \times 40 kV. The low-hybrid wave/current drive (LHW/LHCD) power coupling was optimized using the passive-active multi-junction (PAM) antenna, and the coupled power reached 1.4 MW. The maximum power of the 68 GHz electron cyclotron resonance heating (ECRH) is about 3 MW, and it was successfully applied for the real-time control of neoclassic tearing mode (NTM) on HL-2A [2].

Several diagnostics have been updated or newly developed for turbulence measurement. A beam emission spectroscopy (BES) system [3] has been upgraded to measure local density fluctuations ($k_{\perp}\rho_i < 1$) with the time resolution of $\sim 0.5 \mu\text{s}$ and the spatial resolution of $\Delta r \sim 0.8$ cm and $\Delta z \sim 1.2$ cm, respectively. The measurement array of this system has been expanded to be 24 (radial) \times 2 (poloidal) channels, covering the radial range of $r/a = 0.3\text{--}1.1$. A 32-channel CO_2 laser-based phase contrast imaging (PCI) diagnostic [4] has been developed to measure the line-integrated plasma density fluctuations (covering the radial range of $r/a = 0.6\text{--}0.7$ and wavenumber of $\sim 2\text{--}15 \text{ cm}^{-1}$) with the time resolution better than $2 \mu\text{s}$. For core turbulent electron temperature fluctuation measurement, an eight-channel correlation electron cyclotron emission diagnostic has recently been developed with minimum detectable fluctuation level up to $(\tilde{T}_e/T_e)_{\min} \sim 0.5\%$ and $k_{\theta} < 1.4 \text{ cm}^{-1}$ [5]. A Multi-Color Gas Puff Imaging (MC-GPI) diagnostic [6] has been installed to simultaneously detect two-dimensional electron density and temperature distributions with a spatial resolution of $2.5 \text{ mm} \times 2.5 \text{ mm}$ and temporal resolution of $\sim 100 \mu\text{s}$ in edge plasmas. A new Doppler Coherence Imaging Spectroscopy (Doppler CIS) interferometer [7] has been developed for two-dimensional scrape-off-layer impurity (C^{2+}) flow measurements with a typical temporal resolution of ~ 1 ms. Its spatial resolution is estimated to be up to ~ 0.8 mm in the horizontal direction and ~ 9 mm in the vertical direction, with the field of view of $\sim 34^\circ$.

Over the last several years, the HL-2A team has focused on the investigation of the following areas: (1) Lower-hybrid wave heating and current drive, (2) plasma confinement and turbulent transport, (3) MHD instabilities and

energetic particle physics, and (4) H-mode and ELM control. The highlights of the experimental results are summarized in this paper, while the detailed descriptions can be found in the corresponding references.

Lower-Hybrid Wave Heating and Current Drive

Improvement of Power Coupling of LHW

The LHW system with PAM antenna has been installed on HL-2A and the power coupling during high density H-mode plasma was improved [8]. The hard-X ray measurements [9] indicate that the fast electrons produced by the LHW are located in the plasma core, suggesting the core deposition of the LHW power. Figure 1a shows the coupled power of the LHW system, which reaches 1.4 MW/400 ms under the background of 600 kW NBI-heated plasma (see Fig. 1b). ELM showed up 40 ms after the LHW injection and disappeared as soon as LHW switch-off, as shown in Fig. 1a and c, indicating that the LHW power helps to trigger and sustain ELMy H-mode [10]. The line-averaged plasma density increases significantly from 850 to 930 ms due to the gas puffing with the LHW injection and increases slightly during the steady-state ELMy H-mode phase at 930–1250 ms (see Fig. 1d). Figure 1e shows the loop voltage, which decreases due to the current drive effect. Figure 1f represents the radiation power which significantly increases after the injection of LHW. Figure 1g shows the plasma stored energy. In this case, the reflection coefficient (RC) is pretty low, less than 2%. Since the maximum total output power of the four klystrons is just 2 MW and the transmission efficiency of the transmission line was designed as $\sim 80\%$, the coupled power reaches the floor of the LHCD system ability.

Co- and Counter-Current Drive Experiments

The co-current and counter-current drive experiments have been conducted [10]. The variation of the loop voltage ΔV is widely used to describe the effect of the current drive, which could be described as $\Delta V = |V - V_{\text{LH}}|$. $X = P_{\text{LH}} / (n_e I_p R_0)$ is used to describe the impact of LHCD, which is dependent on the absorbed power P_{LH} (kW), plasma density n_e (m^{-3}), plasma current I_p (kA) and the major radius R_0 (m) for HL-2A. The relation, which depicts the effect of LHW on the current drive, is shown in Fig. 2. In this figure, hundreds of different shots with two directions of the spectra are illustrated. Red triangles are the data from the original direction of the spectra, while blue crosses are the data from the opposite direction of the spectra after the antenna turned around.

Fig. 1 Time evolution of main parameters for 1.4 MW LHW coupling discharge. **a** coupled power of LHW; **b** power of NBI; **c** D_α signal; **d** line-averaged density; **e** loop voltage; **f** plasma radiation and **g** plasma stored energy

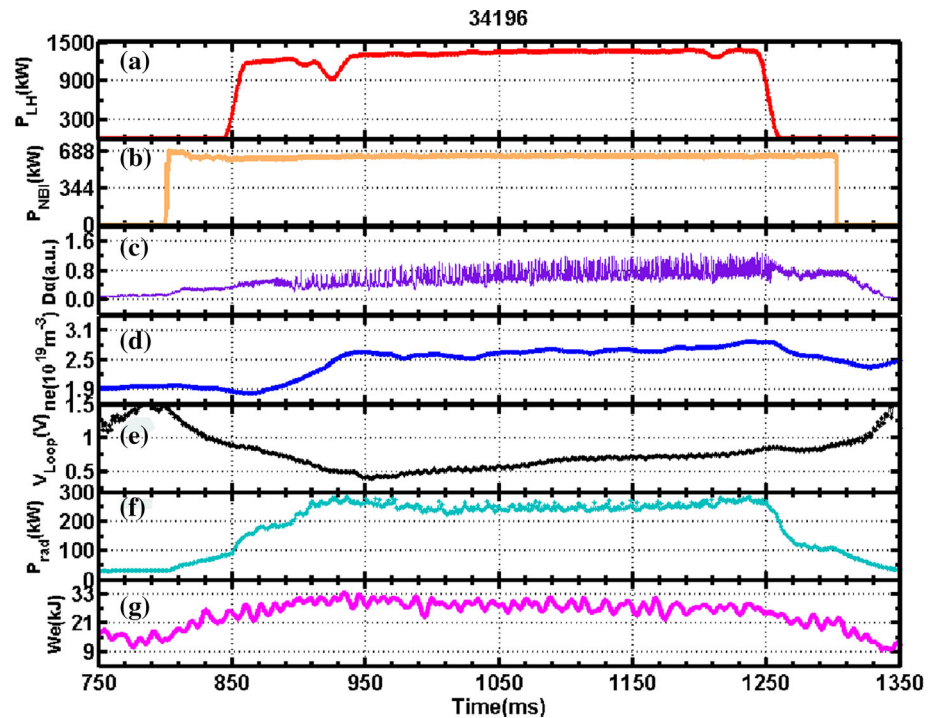
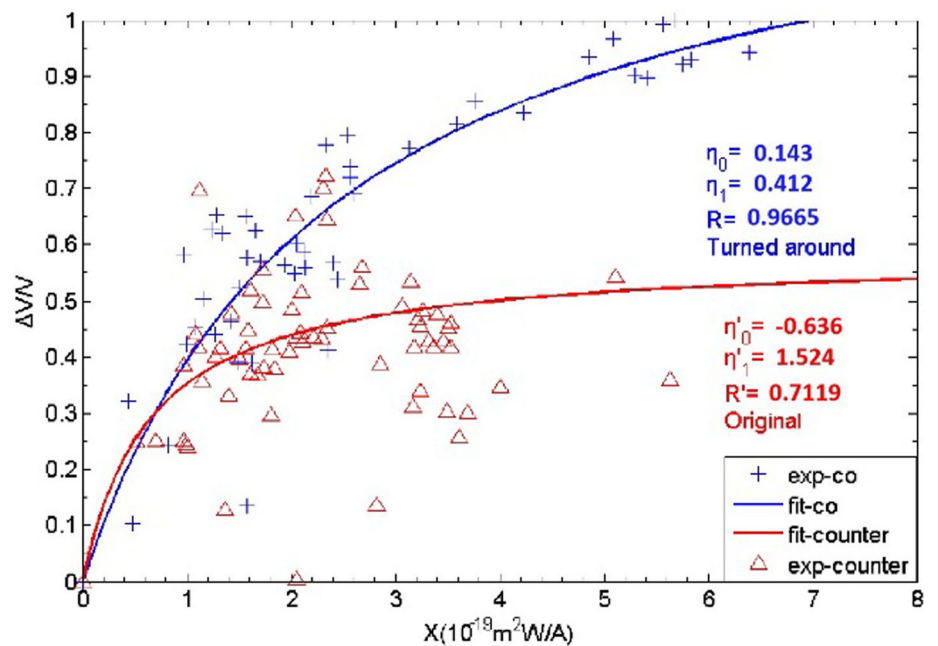


Fig. 2 Statistic of $\Delta V/V$ as a function of $P_{LH}/(n_e I_p R_0)$



In Fig. 2, the two series of data were fitted with the following function:

$$\Delta V/V = X(\eta_0 + \eta_1)/(1 + \eta_1 X)$$

where the η_0 and η_1 represent the LHCD efficiency and the hot effect efficiency, respectively. As shown in the figure, the blue crosses follow the trend of the above fitting function with $\eta_0 = 0.143$ and $\eta_1 = 0.412$. Here, $\eta_0 > 0$ indicates a co-current drive. However, the red triangles and

the fitted curve with $\eta_0 = -0.636$ and $\eta_1 = 1.524$ show a bad correlation. Here, $\eta_0 < 0$ denotes the counter-current drive. The LHCD efficiency was statistically estimated to be $\eta_0 = 0.14 \times 10^{19} \text{Am}^{-2} \text{W}^{-1}$ for the HL-2A experiments, which is quite close to the value estimated above. When the ohmic current is fully replaced by the LHW driven current, $\Delta V/V = 1$ and $\eta_0 = 1/X$, suggesting that the LHCD efficiency is proportional to the plasma density [11].

Full Non-inductive Current Drive

Through the spectrum optimization the full non-inductive LHCD was achieved on HL-2A [12]. Figure 3 shows the evolutions of the main parameters of the typical discharge. The loop voltage in Fig. 3a almost drops to zero and ohmic field current in Fig. 3b becomes flat during 860 kW LHW injection (see Fig. 3c), indicating the full non-inductive LHCD as is shaded by the green box. The LHW reflection coefficient $RC \approx 7\%$. The plasma current at the flat-top phase is about 120 kA (see Fig. 3d). The line-averaged density is about $0.7 \times 10^{19} \text{ m}^{-3}$ shown in Fig. 3e. Both I_p and n_e change very slightly during the LHW injection. The full non-inductive LHCD phenomenon lasts more than 400 ms. The LHCD efficiency was calculated, i.e., $\eta_0 = n_e I_p R_0 / P_{LH} \approx 0.17 \times 10^{19} \text{ Am}^{-2} \text{ W}^{-1}$.

Plasma Confinement and Turbulent Transport

Edge Transport

Two opposite directions of scale-to-scale energy transfer that correlated with the development of turbulence in toroidal plasmas were clarified by means of experimental analysis [13]. In the TPE-RX RFP plasma, the energy cascades forward (directly) from low frequency area to high frequency area, to make the turbulence develop with a broad wavenumber spectrum. In the HL-2A tokamak plasma, turbulent energy concentrates into low frequency area from high frequency region due to inverse energy

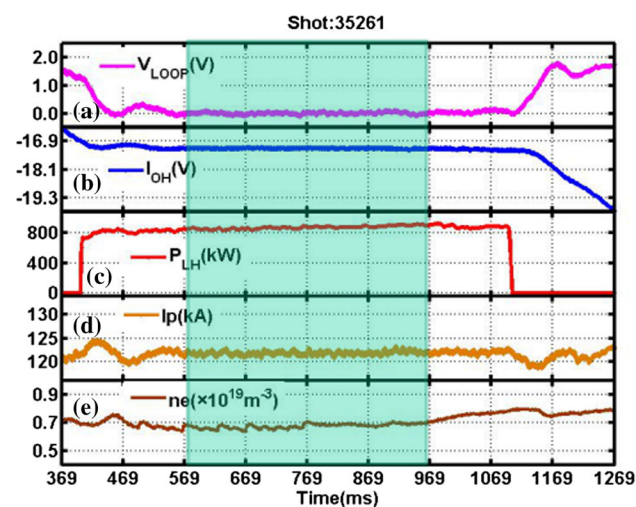


Fig. 3 Full non-inductive LHCD in shot #35261. **a** loop voltage, **b** ohmic field current, **c** coupled LHCD power, **d** plasma current, and **e** line-averaged density. Reprint from [12], with the permission of IOP Publishing

cascade, as shown in Fig. 4. This agrees with theoretical prediction and highlights the modulation mechanism in turbulence which is relevant to the generation of GAM zonal flow.

It has been demonstrated that turbulent kinetic energy transferred from intermediate frequencies (20–80 kHz) into ZFs and GAMs enhances as the heating power is increased [14]. It was also found that the energy transfer rate is small but finite (mostly positive) during L-mode, rises sharply around the L–I transition, and is modulated violently by the 2–3 kHz oscillations during the I-phase. When no strong mean flow was observed to develop during the I-phase, the plasma fell back into L-mode after the LCO phase [15]. Besides, the synchronization of GAM and magnetic fluctuations were identified in the edge plasmas, as shown in Fig. 5. The bicoherence analysis suggests that the MSEFs (mesoscale electric fluctuations) may contribute to the LFZFs (low-frequency zonal flows) formation through the nonlinear three-wave coupling between MSEFs and LFZFs. The frequency entrainment and the phase lock between the MSEFs with components of the dominant GAMs and the $m/n = 6/2$ magnetic fluctuations indicate that GAMs and magnetic fluctuations can transfer energy through nonlinear synchronization [16].

The experimental investigations of the physics linking edge poloidal flows to turbulent momentum transport were performed in Ohmic and ECRH heated L-mode discharges on the HL-2A tokamak. The turbulent Reynolds stress and neoclassical viscosity were found to be the mechanism responsible for the significant deviation of poloidal flow from the neoclassical value. The Reynolds stress can be decomposed into diffusive stress, convection stress, and residual stress, respectively. As a consequence of wave-

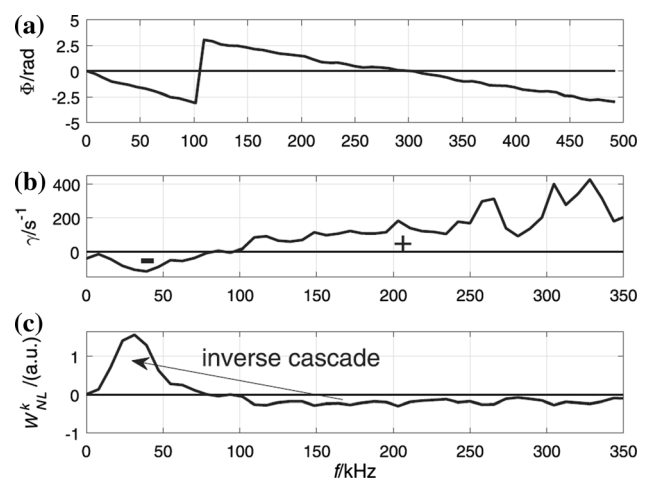
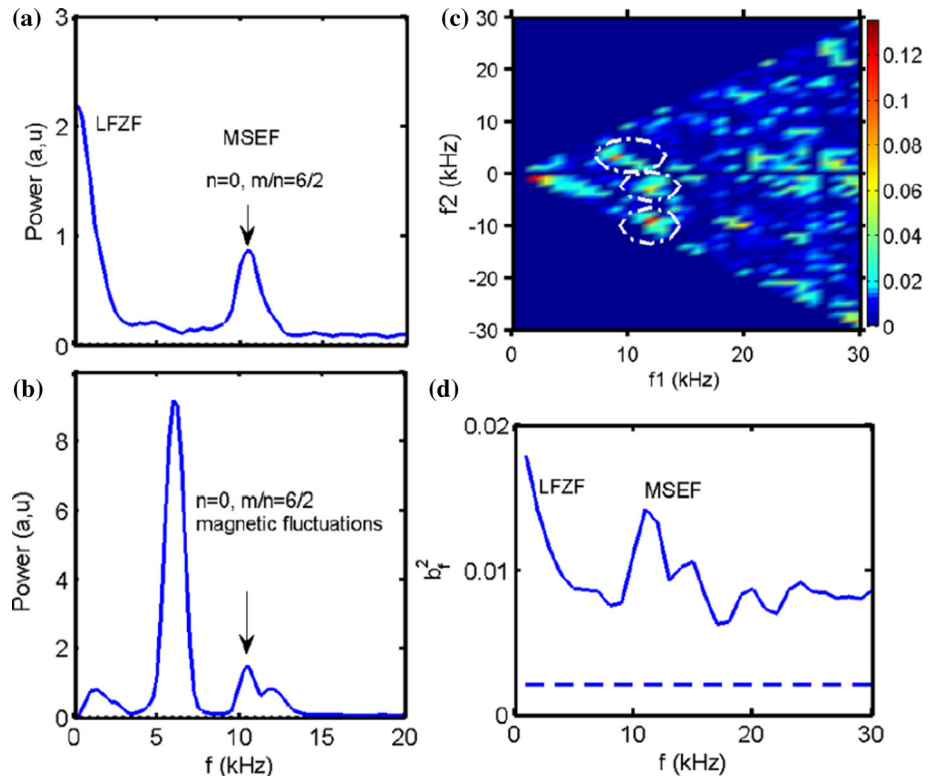


Fig. 4 The experimental analysis results for shot #4206 on HL-2A: **a** the phase spectra Φ , **b** the linear growth rate γ , and **c** the non-linear energy transfer W_{NL}^k as a function of frequency f . Reprint from [13], with the permission of IOP Publishing

Fig. 5 **a** The auto-power spectra of the floating potential fluctuations; **b** magnetic fluctuations; **c** squared bicoherence; and **d** total bicoherence. Reprint from [16], with the permission of APS Publishing



flow momentum exchange, the divergence of residual stress defines an intrinsic poloidal torque that drives the poloidal flow. As shown by Fig. 6, the poloidal torque increases prominently as ECRH power increases. The joint probability distribution function spectra of Reynolds stress

in ECRH L-mode discharges are much broader and more tilted than those in ohmic discharge [17]. These demonstrate that, with plasma heating, turbulence taps the free energy in pressure gradient, and a finite turbulent residual stress develops due to spectral symmetry breaking in turbulence, ultimately leading to the generation of poloidal flow.

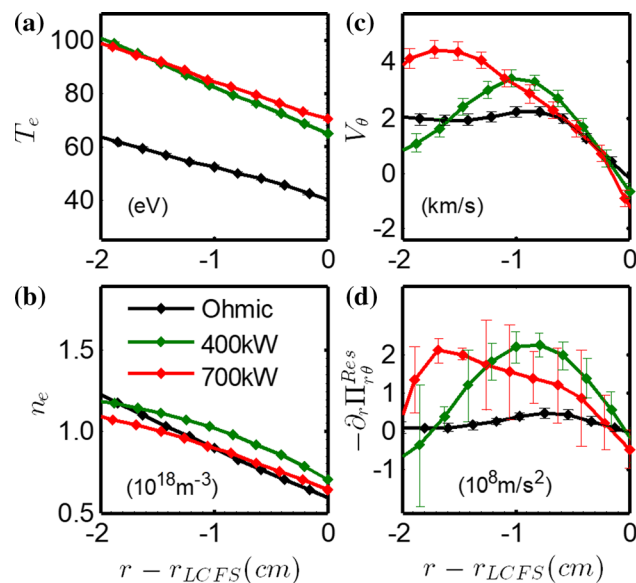


Fig. 6 The experimental results for turbulent generation of edge poloidal flow on HL-2A: **a** Electron temperature; **b** electron density; **c** $E \times B$ poloidal rotation; **d** poloidal torque. Reprint from [17], with the permission of IOP Publishing

In particular, the physics of the symmetry breaking in spectra of edge velocity fluctuations strongly suggests a vital influence of the cross-phase dynamics on turbulent stress. A novel theoretical work indicates that there exist two different states of the cross-phase: slipping and locked state in strong and weak shear regimes, respectively [18]. The relevant experimental study has shown an agreement with this theory by dividing the Reynolds stress directly into fluctuation, cross-phase and coherence [19]. In the strong shear layer, the cross phase is randomly scattered across the layer (phase slipping), and the radial distribution of the Reynolds stress is determined by the cross-phase. In the weak shear region, the cross-phase tends to stay in a coherent state (phase locked), where the fluctuation amplitudes and coherence play a more important role.

Edge turbulent particle transport and shear flows have been investigated as the Greenwald limit is approached in the HL-2A tokamak [20]. As the line-averaged density increases toward the Greenwald limit, the turbulent drive (Reynolds power) of low-frequency zonal flow was observed to decrease with increasing collision rates. The

edge shear layer collapsed and could not regulate turbulent transport efficiently. This may lead to edge cooling and thus the onset of MHD instabilities that limit the density.

Besides, the turbulence-induced zonal flow and pressure-gradient-induced drift were found to play essential roles in the two types of limit cycles (type-Y after L–I transition and type-J before I–H transition), respectively [21]. In type-Y, the turbulence grows first, followed by the localized electric field. In contrast, the electric field leads turbulence in type-J as further discussed later in Sect. 5.1.1.

In the scrape-off layer, turbulent transport is substantially dominated by “blobs”. Blob structures and motions are directly observed in the SOL of HL-2A tokamak by using a gas puff imaging diagnostic [22, 23]. A large blob structure is found to move downward (ion-diamagnetic drift velocity direction) and outward (to the wall) during an L-mode discharge. The high-frequency (> 10 kHz) components are more likely to be the blob structures illustrated in the simulation results based on the theory of interchange instabilities. The generation and propagation process were reconstructed with high spatial and temporal resolutions by using Langmuir probe arrays [24]. The increasing turbulent energy and the spontaneous $E \times B$ flow shear are identified to be responsible for the generation of blobs.

Core Transport

Core Impurity Transport

The impurity concentration will dramatically degrade the plasma performance due to the fueling ion dilution and increased radiation loss. Therefore, the study on impurity transport and its control is extremely important to sustain high plasma confinement in fusion plasmas. In this work, the effect of ECRH on Aluminum impurity transport in the presence of sawtooth oscillations has been investigated with different ECRH deposition locations by the laser blow-off method [25, 26]. When the ECRH power was deposited outside the sawtooth inversion radius, a normal sawtooth oscillation and its precursor mode were observed, whereas an inverse sawtooth crash appeared with the deposition inside the sawtooth inversion radius. A one-dimensional perturbative analysis by STRAHL [27] indicates that for the inner ECRH deposition, both the impurity diffusivity and convection velocity are enhanced in the radial range of $\rho \leq 0.5$ compared to that of the outer ECRH deposition, as shown in Fig. 7. The vertical blue and red lines in the figure denote the locations of the sawtooth inversion radius for the outer and inner ECRH deposition, respectively. In Fig. 7b an outward convection velocity is developed in the core region which plays an important role in flattening the centrally-peaked Aluminum ion density profile. In addition, it is observed that a long-lasting precursor $m/n = 1/1$ MHD mode always exists

in the inner-deposited ECRH discharges, whereas its link with the modification of the impurity transport is not clear yet and needs further survey.

Internal Transport Barriers (ITBs) Formation

The ion internal transport barrier has been observed at the beginning of NBI heating, with the energy confinement time increasing by about 14% [28]. As shown in Fig. 8a and b, the profiles of T_i and v_t peak inside the $q = 1$ surface, which indicates that the barrier foot coincides with the $q = 1$ surface. For steady-state ion ITB, the maximum of the second derivative of ion temperature is considered to be the barrier foot, as remarked by Fig. 8d. The gradient of ion temperature can be up to 17 keV/m during the ITB phase while it is about 7–12 keV/m without ITBs (see Fig. 8c). The $E \times B$ shear in the stationary ITB phase can reach the value for ion temperature gradient turbulence suppression. The simulation results indicate that the ion thermal transport reduced to the neoclassical level inside the ITB region. Besides, the long-lived mode or fishbone driven by energetic ions may play a role in the formation of the large $E \times B$ shear and ion ITBs near the $q = 1$ surface.

Modulation of Electrostatic Turbulence by Large Islands

The multi-scale physics such as the interaction between macro-scale tearing mode and micro-scale turbulence was reported to play a crucial role in the transport regulation in the core of the fusion plasma [29, 30]. The interaction among the $m/n = 2/1$ tearing mode, plasma flow and turbulence has been firstly investigated by utilizing the newly developed electron cyclotron emission imaging (ECEI) system [31] and the Doppler backscattering (DBS) reflectometer [32] in the HL-2A ohmic plasmas [33]. It is observed that the plasma perpendicular flows, flow fluctuations and density fluctuations are all modulated by the rotation frequency of the $m/n = 2/1$ island. The cross-correlation analysis further indicates that the modulation occurs across the island region. The electron temperature gradient drops inside the island and enhances outside the island boundary. As shown in Fig. 9a, in the core region of the island, both of the perpendicular flow and flow shear are quite small, while towards the island boundary the flow increases significantly, leading to the formation of a strong flow shear. For density fluctuations, they decrease inside the island and increase near the island boundary (see Fig. 9b), consistent with the gradient-driven mechanism of the turbulence. These observations provide direct experimental evidence for the latest nonlinear gyrokinetic simulation of multi-scale physics that magnetic island can regulate the local flow shear and turbulence level [34].

Modulation of $m/n = 1/1$ magnetic island on both temperature and density fluctuations was observed during the

Fig. 7 Radial profiles of **a** diffusion coefficient D and **b** convection velocity V for outer- (#22710) and inner-deposited (#22718) ECRH discharges. The vertical blue and red lines denote the locations of the sawtooth inversion radii for the outer and inner ECRH deposition, respectively. The shaded area denotes the error ranges

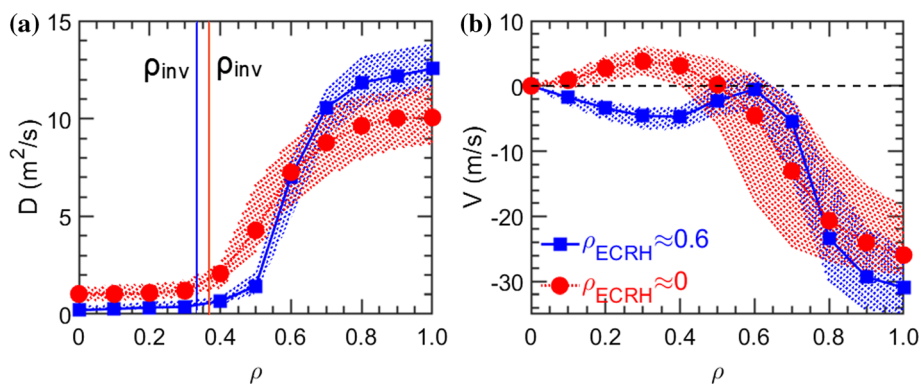


Fig. 8 **a** Radial profiles of ion temperature, **b** toroidal rotation, **c, d** first derivative and second derivative of ion temperature. Reprint from [28], with the permission of IOP Publishing

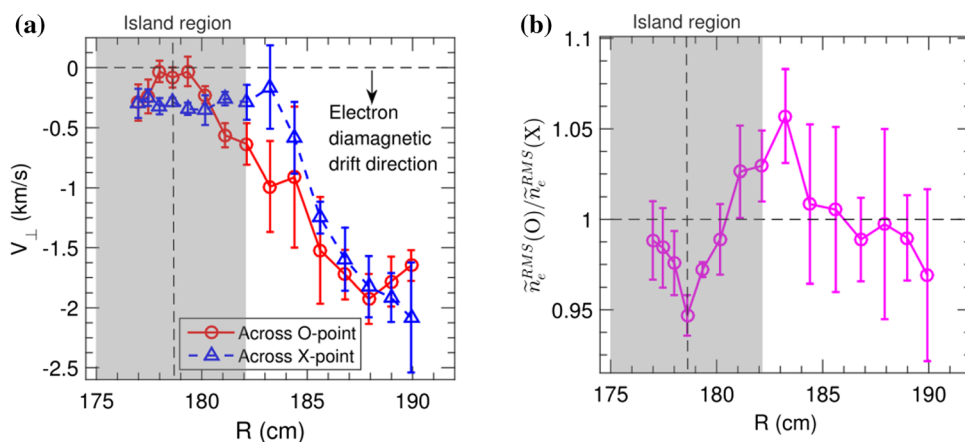
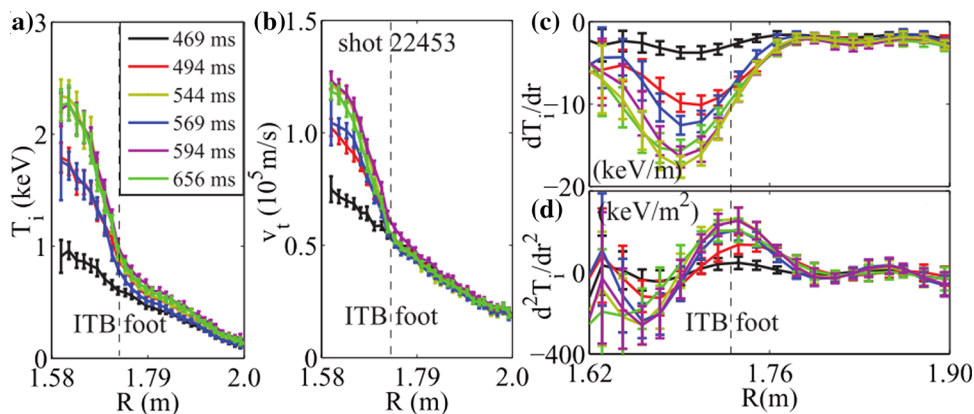


Fig. 9 **a** Radial profiles of perpendicular flow velocity, with red-circle-solid curves and blue-triangle-dashed curves denoting across the O- and X-point, respectively. **b** the change of density fluctuations across the O-point relative to that of across the X-point. The error bars

indicate the standard deviation of the mean values. The island region was shaded in the figure and the vertical dashed line marked the island center. Reprint from [33], with the permission of IOP Publishing

precursor phase of the sawtooth crash [35], as shown in Fig. 10. The amplitude of the turbulence is maximum (minimum) as X-point (O-point) passes by, in agreement with the temperature gradient driven drift wave turbulence. Also, the modulation is confined to the island region and linked to a critical island width ($W_c \approx 4$ cm). The critical island width which also matches the value required for the T_e ‘flattening’, has been estimated in the analytical study [36]

using the parameters at HL-2A. The result indicates that the experimental observation of the critical island width is rather close to that predicted by the theoretical model.

Also, it is found that during the nonlocal transport process the avalanche behaviors are significantly enhanced, characterized by high Hurst parameter, self-similarity and large-scale radial correlations [37]. It is found that the burst of ion fishbone can also induce the non-local thermal transport [38].

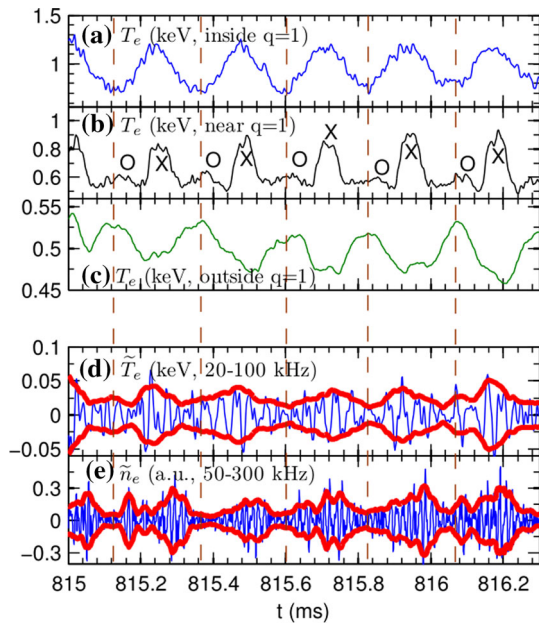


Fig. 10 Temporal evolutions of the ECEI signals measured **a** inside, **b** near, and **c** outside the $q = 1$ surface. **d**, **e** time histories of \bar{T}_e (integrated from 20 to 100 kHz) measured at $R = 182.14$ cm ($\rho \approx 0.33$) and $Z = 3.46$ cm and the line-integral \tilde{n}_e (integrated from 50 to 300 kHz), respectively. The envelopes of fluctuations are depicted by the red curves. Reprinted from [35], with the permission of IOP Publishing

The interplay between nonlocal transport and NTM was firstly observed during the transient nonlocal heat transport event in the HL-2A [39]. Figure 11 illustrates the impact of NTMs on the magnitude of nonlocal transport. After the gas-puffing the nonlocal heat transport phenomenon occurs, leading to a significant increase of the local temperature gradient at the rational surface of $m/n = 3/2$ and hence the onset of the $3/2$ NTM in relatively low β plasmas ($\beta_N < 1$). The NTM, in return, regulates the nonlocal transport by truncation of avalanches (as seen in Fig. 11f, g) by local sheared toroidal flows which develop near the magnetic island. Therefore, the perturbations in the electron temperature after the second gas-puffing are much smaller than that of the first gas-puffing, as shown in Fig. 11b and d.

MHD Instabilities and Energetic Particle Physics

Newly Observed MHD Instability and Alfvénic Modes

Quasi-interchange Mode

For the first time, the formation and evolution of quasi-interchange convection cell have been observed by the

ECEI system on HL-2A tokamak [40], which is shown as Fig. 12. The finger-like structure originates from hot fluctuation gradually and draws into the concave side of the colder crescent at frames (8–14), which exhibits a substitutive characteristic of the quasi-interchange model. The mode propagates in the electron diamagnetic drift direction with an $m/n = 1/1$ mode structure and reduces the stored energy, enhances the divertor D_α signal, which indicates degradation of plasma confinement. Noted that, NIMROD simulations based on experimental data suggest that the typical quasi-interchange mode structure with a hot crescent and a cold bubble can be reproduced when the MHD instability is expressed by the reconstructed two-dimensional electron temperature. Meanwhile, a corresponding mode structure with a cold crescent and a hot bubble, which is made up of the temperature fluctuations, agrees well with the ECEI measurement.

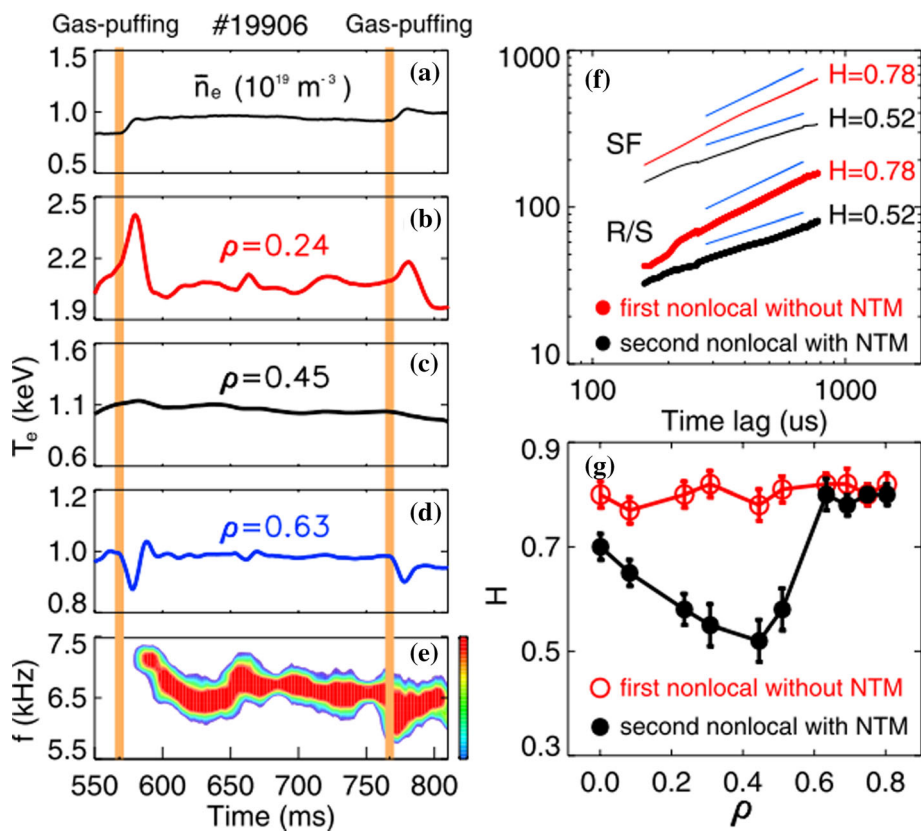
$m/n = 2/1$ Fishbone-Like Modes

Unstable tearing modes are found to interact with energetic-ions and result in amplitude bursting/frequency chirping fishbone-like activities [41], as shown in Fig. 13. The experiments are performed in the NBI heating plasma, where the $m/n = 2/1$ tearing mode is unstable. Interestingly, amplitude bursting and frequency chirping modes are driven unstable during the presence of the conventional tearing mode. The modes propagate in the ion diamagnetic drift direction and induce a strong magnetic fluctuation. The mode numbers are proved to be $m/n = 2/1$ by the Mirnov coil probes, show as Fig. 13e–f. Nonlinear hybrid kinetic-MHD simulations [42] suggest that the co-passing energetic ions are responsible for the drive of the $m/n = 2/1$ mode, and the wave-particle resonance condition meets the condition of $\omega_\varnothing - 2\omega_\theta - \omega = 0$. Here $\omega_\varnothing, \omega_\theta$ and ω are the toroidal, poloidal angular frequencies of energetic-ions and the mode frequency, respectively. These new findings can help to understand the tearing mode induced energetic-particle loss and particle acceleration during the tearing mode reconnection in laboratory and space plasmas.

Non-resonant Internal Kink Mode

Strong non-resonant internal kink modes (NRK) are observed on the HL-2A tokamak. Those ‘non-resonant’ modes are driven by the energetic electrons originated from ECRH + ECCD⁺ [43]. Here, ECCD⁺ means that the driven current direction by electron cyclotron wave is the same as plasma current. The NRKs present different characteristics from the conventional resonant kink modes [44, 45]. The former usually has the saturated amplitude and almost unchanged frequency while the latter is

Fig. 11 **a–e** Time evolutions of plasma density, multi-channel ECE signals and contour-plot of the frequency spectrum in the Mirnov signal showing reduction of nonlocal effects with the presence of the 3/2 NTM; **f** Hurst exponents calculated by SF and R/S methods in \bar{T}_e during two nonlocal phases at $\rho \approx 0.45$; **g** radial profiles of Hurst parameters during the nonlocal phase without (red) and with (black) the NTM. Reprinted from [39], with the permission of Nature Publishing



characterized by the periodic strong bursting amplitude and rapid chirping frequency. Figure 14 shows a typical example of NKM measured by the ECE system. Theoretical analysis based on the dispersion relationship [46] suggests that the NRK is unstable only when the minimum safety factor is beyond unity, but it will be stable in the case of q_{min} larger than a certain value. Moreover, the mode frequency is found to be proportional to q_{min} , which agrees well with the experimental observation.

BAE, KBM and AITG Modes

Beta induced Alfvén eigenmodes (BAEs), one of the continuum gap modes, have also been detected on the HL-2A tokamak [47]. The BAEs are usually excited in the cases of q_{min} larger or smaller than unity. The most unstable mode numbers are $n = 2-3$ and the mode frequencies are around 60–95 kHz. The BAEs are highly localized at the core region and the radial mode structures have been detected by the multi-channel microwave reflectometer, shown as Fig. 15. The reflectometer launches 34–40 GHz microwaves into plasma and the cutoff layers of the microwave can be determined with the density profile measured by the frequency modulated continuous wave reflectometer. In Fig. 15b, the density fluctuations are filtered by the numerical pass-band filter with a frequency of 90–95 kHz.

The mode is found to localize at the region of $\rho = 0.07-0.26$. The BAEs will suffer from stronger ion Landau damping in the high density discharge, and therefore, they are only unstable in plasmas with a density lower than $1.2 \times 10^{19} \text{ m}^{-3}$ on HL-2A tokamak.

In the BAE frequency region, there are two other instability branches, i.e., the kinetic ballooning modes (KBMs) and Alfvénic ion temperature gradient (AITG) modes [48]. The former is usually driven by the plasma pressure gradient and belongs to the energetic-particle mode family because its frequency depends strongly on energetic properties [49]. The mode frequencies are characterized by $\omega_{*pi}/2 < \omega < \omega_{*pi}$, where ω_{*pi} is the ion diamagnetic drift frequency. The latter originates from finite ∇T_i effects due to wave-particle interactions with thermal ions via geodesic curvature coupling, which is most unstable when the condition $\Omega_{*ip} \sim q\sqrt{7/4 + \tau}$ is fulfilled. Here, $\Omega_{*ip} = \omega_{*ip}/\omega_{ti}$ and $\tau = T_e/T_i$. This can be understood as a branch connecting KBM (diamagnetic effects $\Omega_{*ip} \gg q\sqrt{7/4 + \tau}$) and BAE (ion compression effects $\Omega_{*ip} \ll q\sqrt{7/4 + \tau}$). It is found that the AITG modes become more unstable when the magnetic shear is smaller in the low pressure gradient regions [50]. The interaction between AITG activity and energetic particle also needs to be investigated with greater attention in fusion plasmas,

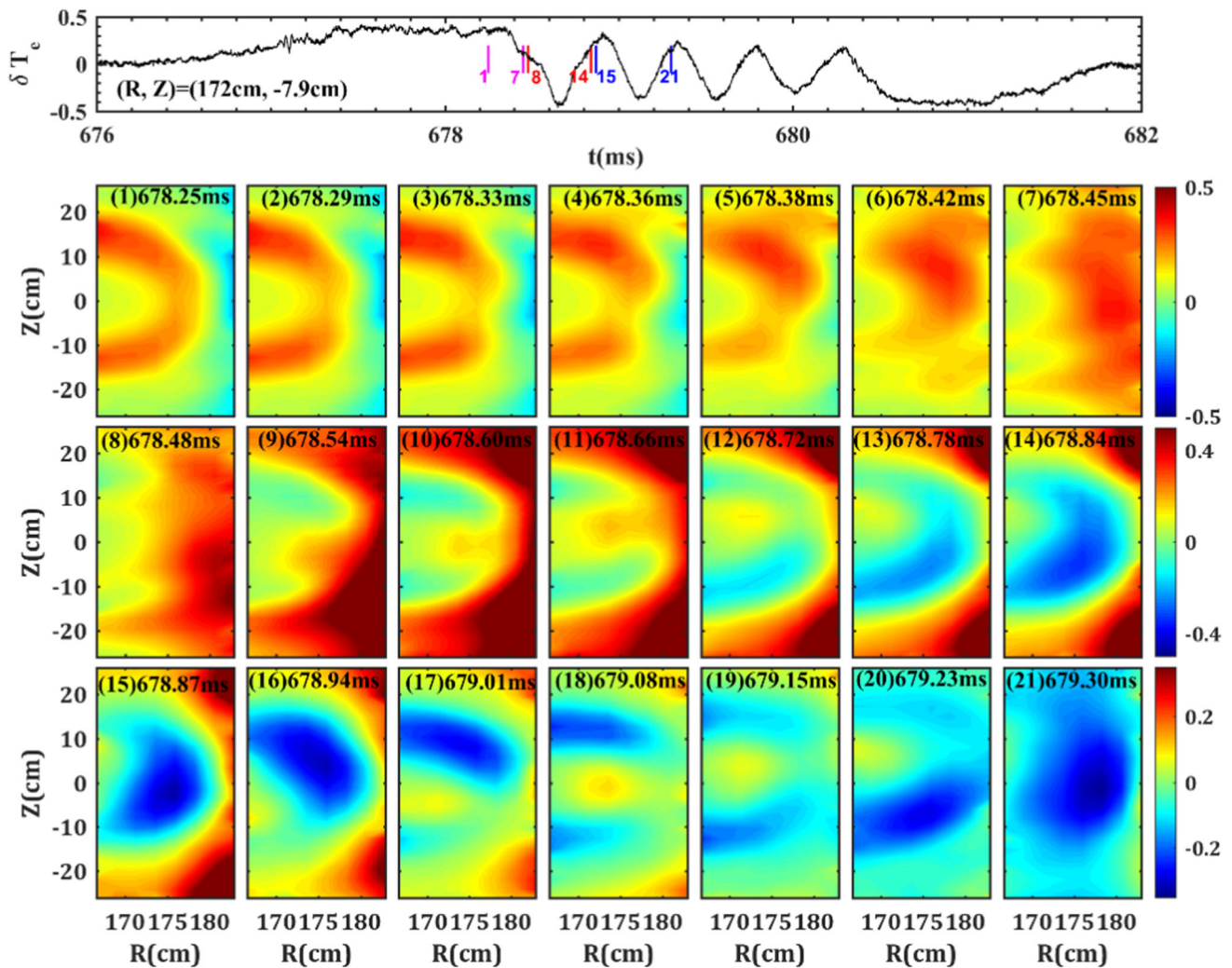


Fig. 12 Two-dimensional temperature fluctuation imaging is given by the ECEI system. Frames (1–7) show the fluctuation before the plasma collapse, frames (8–14) present the formation of quasi-interchange convection cell, and frames (15–21) exhibit the evolution of the mode in a complete period. The normalized temperature

fluctuation at $(R, Z) = (172 \text{ cm}, -7.9 \text{ cm})$ is shown at the top of the figure. The moments of frame (1), (7), (8), (14), (15), and (21) have been marked out. Reprinted from [40], with the permission of AIP Publishing

since these fluctuations can be enhanced by weak magnetic shear and energetic particles.

Nonlinear Interaction Between MHD Instability and Alfvénic Modes

There are two routes for the nonlinear dynamic evolution of Alfvénic fluctuation [51], i.e. wave-particle and wave-wave interactions. The nonlinear wave-particle resonance can lead to a frequency chirping behavior while the wave-wave interaction usually performs as mode–mode coupling. Here, our attention is devoted to nonlinear interaction between MHD and Alfvénic modes by the method of wave-wave coupling. Figure 16 shows a typical example of nonlinear mode coupling [52]. A series of MHD instabilities, including Alfvénic modes (AMs, 90–160 kHz,

consisting of TAEs with finite toroidal mode number and an $n = 0$ mode), high frequency modes (HFMs, 230–250 kHz) and tearing mode (about 10 kHz) can be observed in the spectrogram of the magnetic signal. Differences in frequency and mode number of two adjacent AMs are comparable to the tearing mode frequency and toroidal mode number, i.e. $|f_{AM1} - f_{AM2}| = f_{TM}$ and $|n_{AM1} - n_{AM2}| = n_{TM}$, which reveals a nonlinear mode coupling process between the AMs and tearing mode. Especially, the high frequency mode in the ellipticity-induced Alfvén eigenmode (EAE) frequency region is an axisymmetric mode with a toroidal mode number of $n = 0$. The squared bicoherence reveals that the TAE firstly nonlinearly interacts with the tearing mode and results in the generation of other sidebands. Then two TAEs propagating in different directions but with the same mode number

Fig. 13 Typical discharge parameters with TMs and fishbone-like activities during NBI heating on HL-2A. From top to bottom, **a** plasma current I_p , line-average electron density and NBI power, **b** soft x-ray signal, **c** magnetic probe signal, **d** enlarged Mirnov signal during a burst, and **e** and **f** poloidal and toroidal mode-numbers. Reproduced courtesy of IAEA. Figure from [41]. Copyright 2018 IAEA

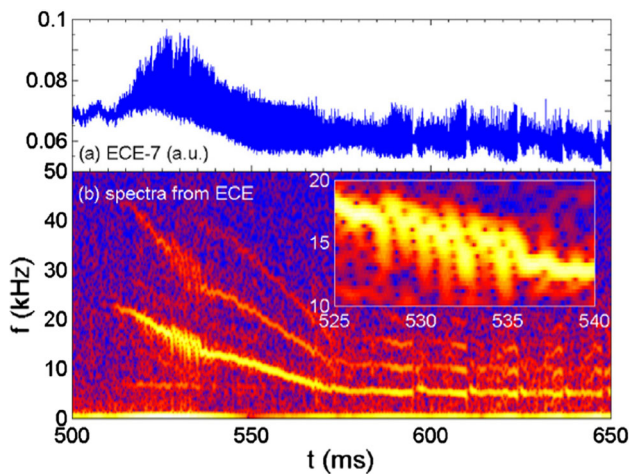
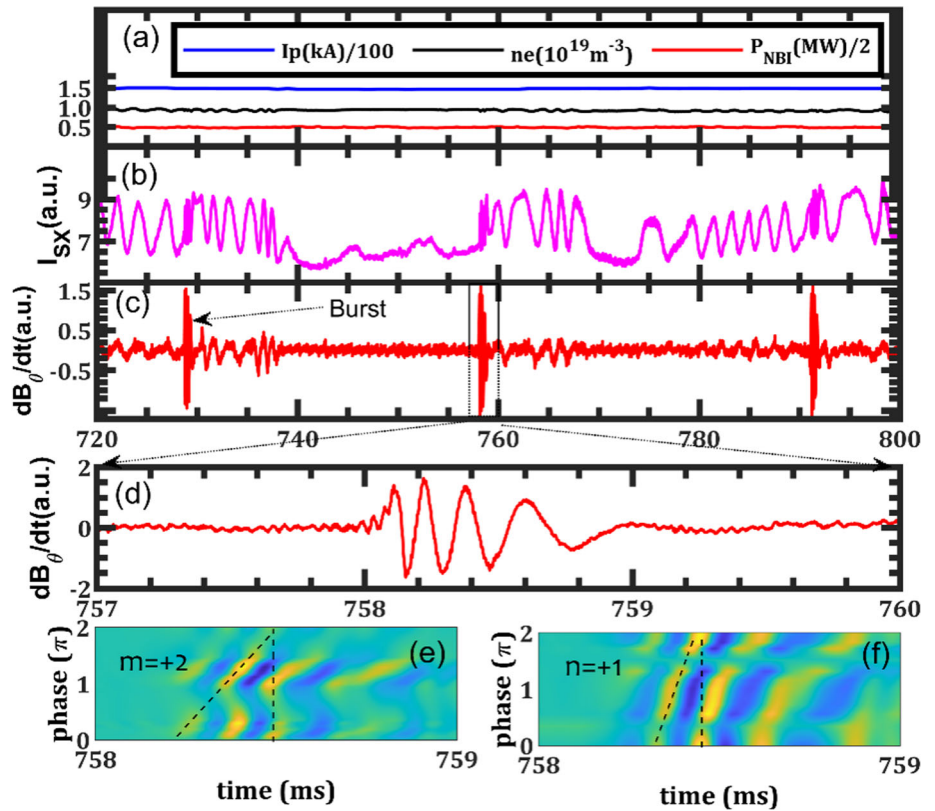


Fig. 14 Strong energetic-electron-induced NRK during on-axis high power ECRH + ECCD⁺ in shot #24067. **a** ECE signal with $r = 7.3$ cm **b** spectrogram of ECE signal. Reprinted from [43], with the permission of IOP Publishing

couple together and give rise to the axisymmetric mode. The mode excited through nonlinear interaction is expected to have a global characteristic due to low poloidal/toroidal mode numbers, but the excitation mechanism is remarkably different from the two existing theoretical models [53, 54]. The high frequency $n = 0$ mode appears as an energy transfer channel during the nonlinear procedure and it can

cause the growth of MHD instability with finite toroidal mode number via beating with tearing mode. Besides, other two kinds of axisymmetric magnetic modes, which are also driven by nonlinear mode coupling, appear in the presence of strong tearing modes on HL-2A [55]. One has been identified as an energetic geodesic acoustic mode (EGAM) while the other is found firstly in the range of TAE frequency, due to nonlinear couplings of tearing modes with BAEs and TAEs, respectively. Except for nonlinear couplings of TAE/BAE and $m/n = 2/1$ tearing mode near $q = 2$ surface, other kinds of multi-scale interactions have also been observed recently in the HL-2A core NBI plasmas, including the synchronous coupling between $m/n = 1/1$ kink mode and $m/n = 2/1$ tearing mode, AITG/KBM/BAE and $m/n = 1/1$ kink mode near $q = 1$ surface, and between $m/n = 1/1$ kink mode and high-frequency turbulence [30]. Multi-scale interactions via the nonlinear modulation process are found to cause the drop of ion temperature and rotation frequency, it may also enhance plasma transport and trigger sawtooth-crash onset. More attention should be paid to the multiple modes phenomenon.

Suppression and Mitigation of MHD Instability and Alfvénic Modes

MHD instability and Alfvénic modes not only reduce plasma confinement, but also harm the fusion devices

Fig. 15 **a** The cutoff layers of 34–40 GHz microwave determined with the density profile (dark diamonds) measured by the frequency modulated continuous wave reflectometer and **b** two-dimensional density fluctuation. The density fluctuations are filtered by the numerical pass-band filter with a frequency of 90–95 kHz. Reprinted from [47], with the permission of IOP Publishing

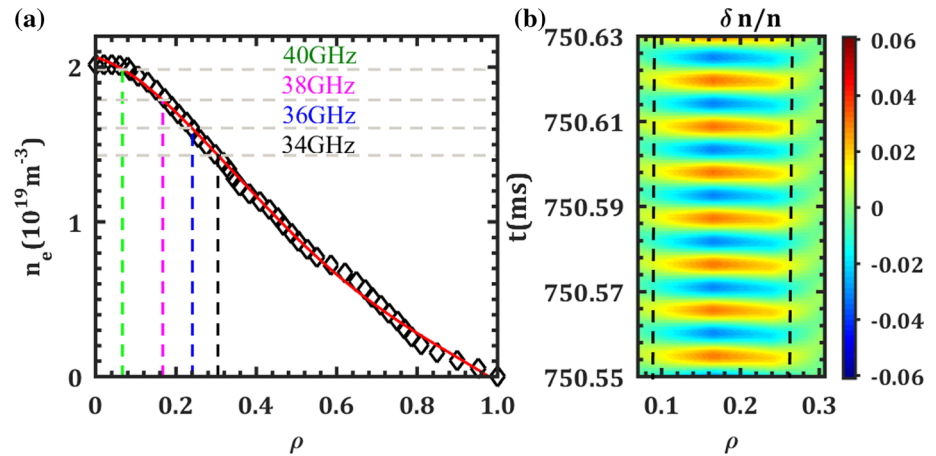
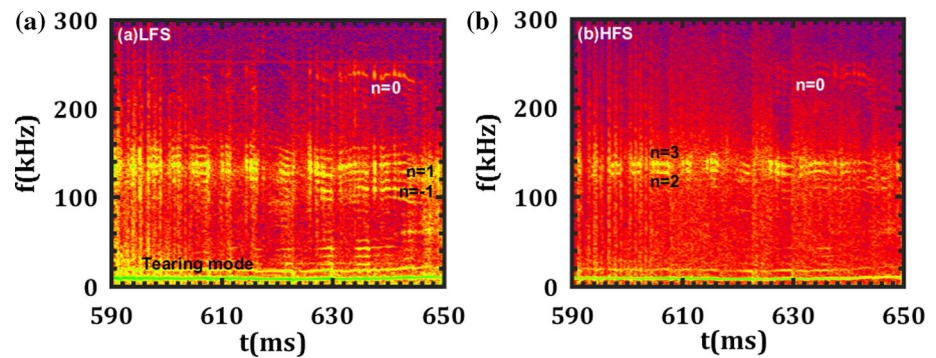


Fig. 16 Alfvénic modes nonlinearly couple with tearing mode at the spectrogram of the magnetic signal in **a** low field side and **b** high field side. Some modes are labeled with corresponding toroidal mode numbers. Reprinted from [52], with the permission of IOP Publishing



[56, 57]. It needs to take urgent steps to control electromagnetic instabilities. The three-dimensional magnetic perturbation fields and ECRH/ECCD are the most possible candidates for suppressing or mitigating MHD instability and Alfvénic modes in the future burning plasma [58, 59]. To control the neoclassical tearing modes (NTMs), which may limit the stability and performance of plasmas, a real-time control system based on ECRH have been developed on HL-2A tokamak [2]. The control system combines real-time diagnostic system, reflective memory (RFM) and ECRH system. The system is utilized to control conventional tearing modes, shown as Fig. 17. In the experiment, the ECRH with an input power of 300 kW is turned on after the amplitude of the tearing mode reaches the threshold. Note that the launcher mirror rotates from an initial angle to the target angle and it enables the ECRH power deposition varying from $\rho_{ECRH} = 0.1$ to $\rho_{ECRH} = 0.6$. The mode amplitude restores when the power deposition is far away from the $q = 2$ rational surface. The mode can be completely suppressed when the ρ_{ECRH} exactly matches the magnetic island location ρ_{island} .

Stabilization of the energetic ion driven fishbone modes by electron cyclotron resonance heating (ECRH), is observed for the first time in a toroidal plasma [60]. The effect depends not only on the injected power but also on

the radial deposition location of ECRH, shown as Fig. 18. As shown in the figure, at the same power level, when the ECRH power is deposited at $\rho_d = 0.42$, the fishbone modes are fully suppressed while partly mitigated at $\rho_d = 0.02$ and 0.66. When the deposition location is fixed at $\rho_d = 0.42$, the stabilization effect becomes more and more remarkable when the ECRH power increases gradually. The fishbone modes can be completely suppressed when the injected ECRH power level exceeds a certain threshold of 0.6 MW. The underlying mechanism is explored with the fishbone dispersion relation including the resistive effect. The result suggests that the magnetic Reynolds number plays a key role in the mode stabilization and it weakens the mode growth rate and enhances the critical energetic ion beta without changing the energetic ion population.

H-Mode and ELM Control

High confinement mode (H-mode) is envisaged as an alternative standard operation scenario on future reactors like ITER. It is generally accessed through the formation of the transport barrier at the plasma edge from the low confinement mode (L mode) and it often characterized with

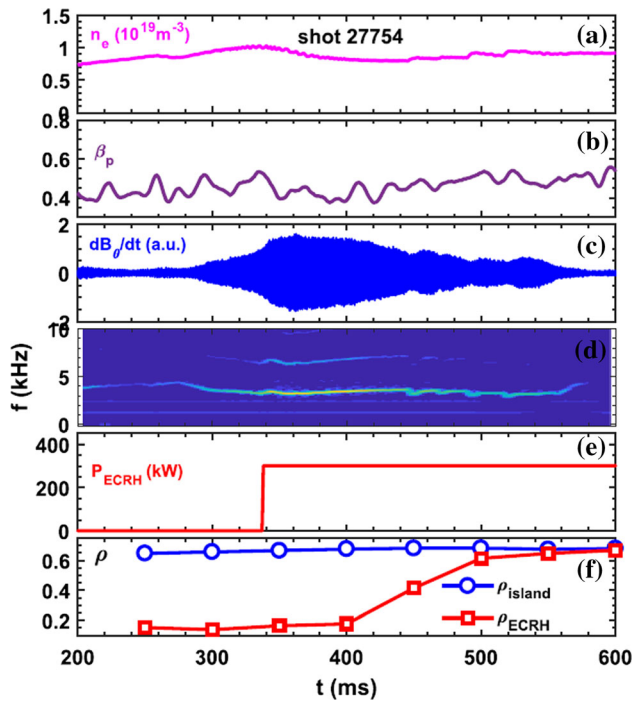
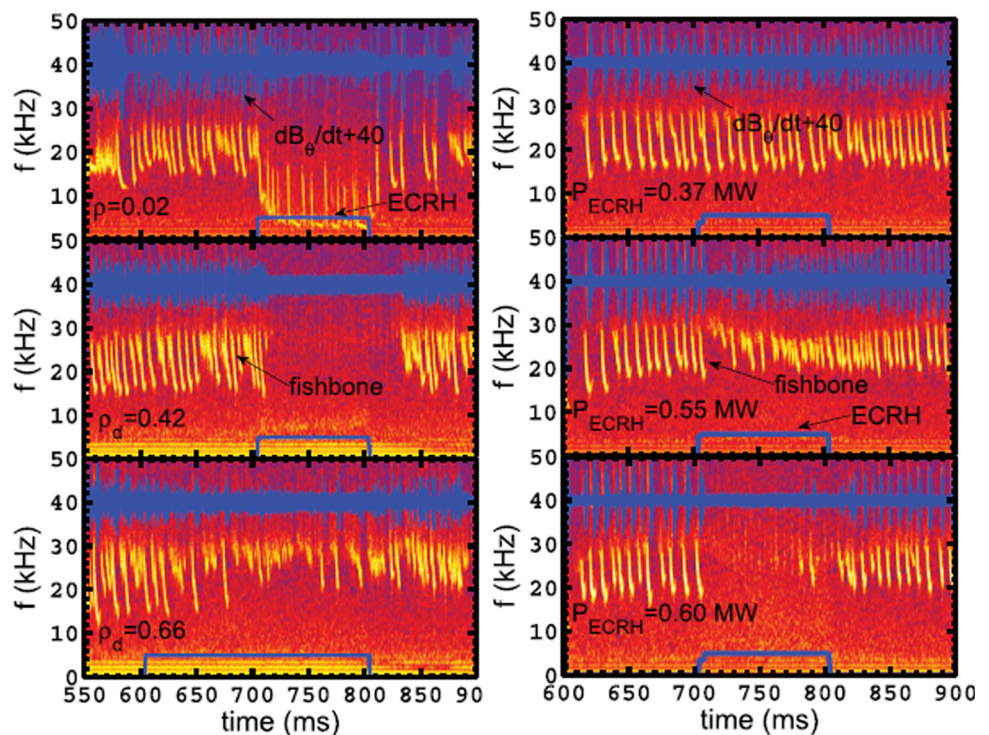


Fig. 17 Tearing mode was killed by ECRH in real-time with the steerable mirroron HL-2A. **a** Line-averaged density, **b** poloidal beta, **c**, **d** Mirnov magnetic perturbation and its frequency spectrum, **e** ECRH power **f** the positions of 2/1 magnetic island (ρ_{island}) and ECRH power deposition (ρ_{ECRH}). Reprinted from [2], with the permission of AIP Publishing

Fig. 18 Effects of ECRH on the stability of ion fishbone activities. Same ECRH power $P_{\text{ECRH}} = 1.0\text{MW}$, but the different deposited location (Left column); Same deposited location $\rho_d = 0.42$, but different ECRH power (Right column). Reprinted from [60], with the permission of IOP Publishing



the edge localized modes (ELMs), which release a large number of particles and energy of the pedestal [61]. Thus, the physics of transition from L mode to H-mode and maintaining of the H-mode have been extensively investigated. During H-mode, the plasma performance would be affected by the abundant pedestal instabilities, especially the edge localized mode. This section reports the studies of H-mode related physics on HL-2A in recent years, including L–I–H transition physics, the instabilities during H-mode, the control of the instabilities especially the ELM control physics with different techniques.

Physics of L–H Transition

Dynamics During the L–I–H Transition

Two types of LCO in the I-phase of the L–I–H transition were found for the first time in the low-intermediate-high (L–I–H) confinement mode transition experiments [21]. The Type-Y LCO appears at the early stage of I-phase, while Type-J LCO is towards the end of I-phase prior to the I–H transition. The time evolution of D_α signal is shown in Fig. 19a. Plasma gradually evolves from the L-mode into the I-phase, and finally transitioned into the H-mode, where the bars with different colors indicate the different time intervals in each stage of the plasma. Figure 19b shows the

phase diagram between the normalized radial electric field oscillation and the envelope of density fluctuations, where different colors correspond to different time intervals as indicated in Fig. 19a. Both the density and electric field were measured by the Langmuir probe array at the mid-plane at the low field side. The probes were inserted about 1 cm inside the last closed flux surface. The envelope of density fluctuations leads the radial electric field oscillation (clockwise rotation), and the modulation of turbulence by the LCO is strong in the early stage of the I-phase (blue color). However, at the later stage (in green and black colors) of the I-phase, the radial electric field grows first and leads to the change in the envelope of density fluctuations (counter-clockwise rotation). The LCOs, which are not driven by turbulence, seem to be critical in triggering the I-H transition. It should be concluded that two predator–prey regimes might coexist for ‘zonal flow–turbulence’ and ‘turbulence–pressure gradient (∇P)’ interactions [21]. In this paradigm, the first interaction involves the zonal flow and turbulence. Zonal flows are the predator and turbulence is the prey. It extracts energy out of turbulence and also inversely regulate and suppress turbulence via flow shearing. The second predator–prey regime involves turbulence and pressure gradient (∇P), where turbulence is the predator and ∇P is the prey. A large ∇P leads to a high level of turbulence and turbulent transport, resulting in a reduction in ∇P and turbulent transport (due to weaker driving). Then the reduced

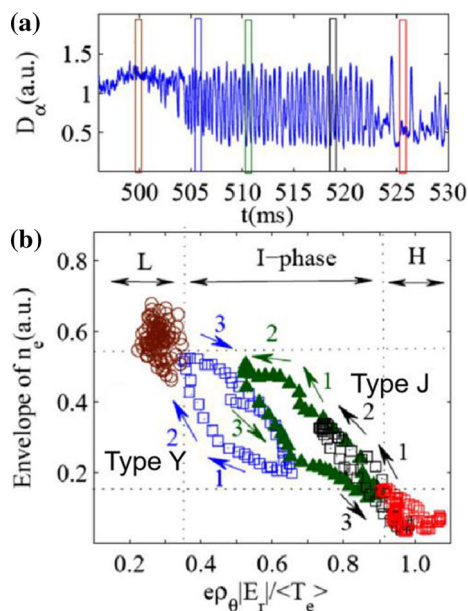


Fig. 19 **a** Evolution of D_α emission; **b** Lissajous diagram between normalized radial electric field and the envelope of density fluctuations in the phase space. Different colors show different periods as indicated in **(a)** by five bars (shot #19299). The numbered arrows denote the time sequence in each period. Reprint from [21], with the permission of APS Publishing

turbulent transport leads to a large ∇P again. This forms a loop and hence becomes the second predator–prey regime.

In the recent experiments on HL-2A, the dynamics of the edge plasma flows and turbulence during the L–I–H transition by using Doppler reflectometry [62]. Figure 20 is the time evolution of the spectrogram of E_r fluctuation measured by the 50 GHz X-mode Doppler reflectometer. During the L-mode regime, GAM, which has been identified by its acoustic property and poloidal and toroidal symmetry on HL-2A, is observed, and its frequency is about 10–15 kHz as shown in Fig. 20b. The GAM frequency, which is proportional to the acoustic speed, thus the plasma temperature, increases slightly during the NBI heating phase as shown in Fig. 20a, where the plasma temperature is increasing. Figure 20b and c shows the power spectrum of E_r fluctuation at $t = 537$ ms and at $t = 551$ ms, respectively. It could be observed that LCO is generated, and the intensity of GAM is gradually decreased after the L–I transition. The GAM and LCO coexist for a short time of a few milliseconds during this phase as shown in Fig. 20c. The coexistence of the GAM and LCO suggests that these two oscillatory flows and turbulence could have nonlinear interaction or energy transfer between them, which is demonstrated by the bi-spectrum analysis. However, the GAM and LCO disappear in the H-mode plasma. Instead, an increase of $E \times B$ shear flow has been observed with pedestal turbulence reduction before the I–H transition. The results seem to indicate that the increased mean $E \times B$ shear flow plays a key role in turbulence

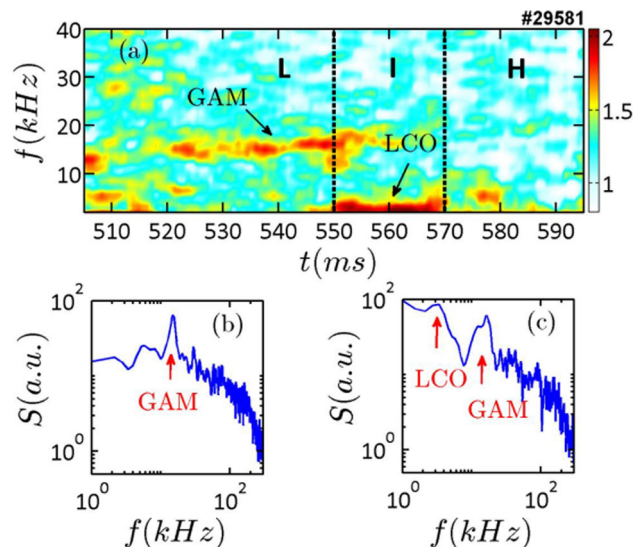


Fig. 20 **a** Spectrogram of E_r fluctuation measured by the 50 GHz X-mode Doppler reflectometer. **b** The power spectrum of E_r fluctuation in the L-mode at 537 ms with GAM. **c** The power spectrum of E_r fluctuation in the I-phase at $t = 551$ ms with the coexistence of GAM and LCO. Reprint from [62], with the permission of AIP Publishing

suppression and also leads to the disappearance of the GAM and LCO flows [62]. It should be also demonstrated that the increase of the mean $E \times B$ shear flow prior to the two transitions mainly results from the ion diamagnetic component.

Critical Velocity Shear Flow for Triggering L–H Transition

An analysis of two discharges with identical plasma parameters shows that the velocity shear must increase to a critical value to permit the L–H transition, meaning that the critical value functions as a velocity shear threshold for the L–H transition [63]. In addition, the parametric dependence of the critical value on the plasma parameters shows that the critical velocity shear remains almost constant as the density varies and independent of the total heating power. Similar results on the density independence have also been observed in ASDEX-U [64] and in JET [65].

Two discharges with identical plasma parameters but different L–H transition times are compared, as shown in Fig. 21. The D_α signal in Fig. 21a shows that the discharge #29813 transits from the L-mode into the I-phase at around $t = 540$ ms, and then goes into the H-mode at about $t = 560$ ms. The D_α signal in Fig. 21b shows the discharge #29706 transits into the I-phase at $t = 565$ ms and the I–H transition happens at $t = 582$ ms. Figure 21c shows the time evolution of the velocity shear in the pedestal region for discharges #29813 (blue) and #29706 (red). Although the transitions happen at different times, it should be noted that the values of the velocity shear are nearly the same, the velocity shear at the L–I transition is about $|\partial u_\perp / \partial r|_{L-I} \approx 80$ kHz and the velocity shear at the I–H transition is about $|\partial u_\perp / \partial r|_{I-H} \approx 120$ kHz. The results suggest that there is a critical velocity shear value for the L–H transition.

The result suggests that a critical velocity shear must be achieved for the L–H transition to occur and that different levels of heating power are required to achieve such critical values under different plasma densities.

L–H transition stimulated by SMBI

As mentioned above, pedestal dynamics such as the interaction between GAM and turbulence can play an important role in L–H transition. This is once confirmed during the L–H transition experiment stimulated by SMBI [66]. It has been found that SMBI could stimulate two dynamic processes (GAM enhancement and turbulence regulation), and therefore quench the turbulence and maintain the turbulence collapse. Thus, turbulent transport is reduced and the L–H transition is triggered.

To demonstrate the effect of SMBI on the L–H transition, the SMB injection time for plasmas with identical discharge parameters is scanned as shown in Fig. 22. The

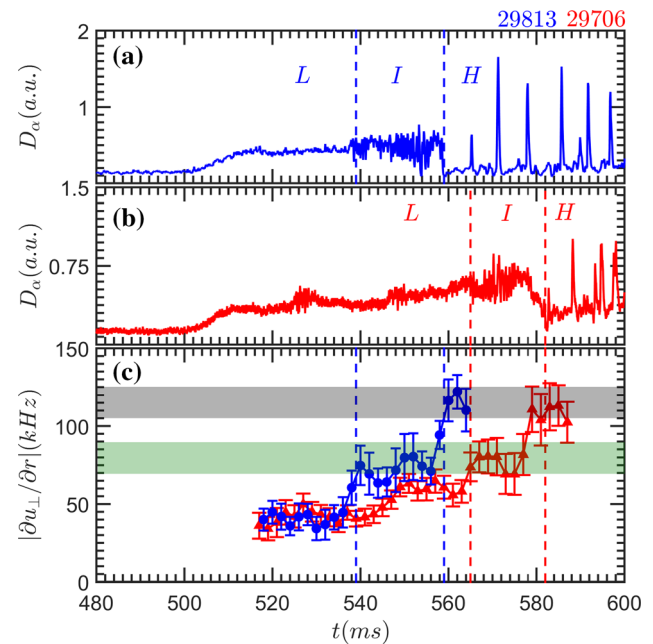


Fig. 21 Time traces of: **a** D_α intensity of #29813, **b** D_α intensity of discharge #29706 and **c** velocity shear of discharges #29813 (blue) and #29706 (red). Reprint from [63], with the permission of IOP Publishing

pulse duration of SMBI is 2 ms. As shown in Fig. 22a, the NBI power is about 1 MW which is close to the marginal H-mode power threshold of the HL-2A. For the shot of 27,882, the SMB is injected at 543 ms as shown in Fig. 1e and then the plasma transits into the ELMy H-mode after 10 ms when the plasma density reaches $1.85 \times 10^{19} \text{ m}^{-3}$ as shown in Fig. 1b. When the injection time of SMB is intentionally postponed to 593 ms in the shot of 27887, the plasma also transits into the H-mode after about 10 ms, and the plasma density at the transition is $2.2 \times 10^{19} \text{ m}^{-3}$ herein. The results show that the L–H transition follows the SMBI pulse. The further analysis determines that the L–H transition is not due to the increasing plasma density [66].

Achievement and Maintenance of high performance H-mode plasma

Understanding of L–H transition physics also helps to achieve high performance H-mode plasma discharge. During the H-mode of magnetically confined devices, the pedestal plays a key role in governing the performance of the core plasma by providing a boundary condition for the stiff core transport. Thus, it is essential to study the pedestal dynamics and understand the underlying physics for the maintenance of high performance plasma. This section reports the studies of the H-mode instability that have a significant impact on the performance of plasma such as electromagnetic instability driven by impurity gradient and

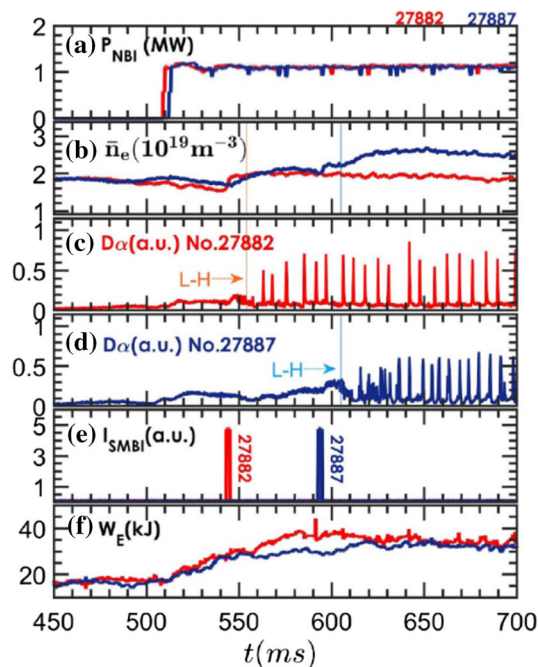


Fig. 22 Comparison of two H-mode discharges stimulated by SMBI at different times. **a** NBI heating power, **b** line-averaged electron density, **c** divertor D_α signal of shot #27887, **d** divertor D_α signal of shot #27882, **e** monitor of SMBI pulses for these two shots, and **f** stored plasma energy. Reprint from [66], with the permission of IOP Publishing

quasi-coherent modes. In particular, ELMs control will be emphasized in the next section.

Achievement of high beta (β_N) H-mode discharge on HL-2A

Investigation of the physics in burning plasma requires the high beta operation with the high bootstrap current. Since the first H-mode discharge on HL-2A, the parameters of H-mode discharge consecutively increase with growing heating power and control techniques. In the latest experimental campaign, HL-2A has firstly achieved the H-mode discharge with the normalized beta $\beta_N > 3$ as shown in Fig. 23. In this experiment, a newly developed NBI heating system on HL-2A is applied besides the original one. The toroidal field for this discharge is about 1.3 T, and the q_{95} is about 3.7. The total heating power is 1.8 MW, 1.3 MW of which is sustained by these two NBI systems as shown in Fig. 23a and the LHW system provides the rest 0.5 MW. The plasma current in Fig. 23b and the line-averaged density in Fig. 23c are 160 kA and $2.5 \times 10^{19} \text{ m}^{-3}$, respectively. The ELMs spikes are represented by the D_α signal in Fig. 23d, which shows that the plasma is in the H-mode phase from 850 to 1600 ms. In Fig. 23g, it was observed that the normalized beta is higher than 2 during the whole H-mode phase and it is over 3 for a very short time. The reason why the high plasma beta (> 3) is not

sustainable might be due to the formation of the edge transport barrier.

Electromagnetic Instabilities in H-Mode Plasmas

In HL-2A, it has been found that the impurity accumulation would also have a significant impact on pedestal dynamics and result in the H–I transition [67]. Figure 24a shows the repetitive H–I transition by divertor D_α signal. The plasma stored energy and the density also change along with the transitions. The experimental results showed that, during the H-mode phase, the impurity gradually accumulated at the edge plasma region (Fig. 24c), where n_z is the effective impurity density deduced from the bolometer array that is mainly contributed by intrinsic impurity. The turbulence was strongly excited by the accumulation of impurity at the plasma peripheral region as shown by a broadband (frequency of 50–150 kHz) electromagnetic turbulence from the spectrogram of magnetic fluctuations (Fig. 24d). Then, the impurity was immediately exhausted, and the plasma transitioned into the I-phase, with the generation of electrostatic turbulence modulated by limit cycle oscillations. With the gradually increasing pedestal pressure gradient during the I-phase, the plasma returned to the H-mode regime. This suggests that electromagnetic turbulence plays a key role in the cyclic transitions between the I-phase and the H-mode.

Quasi-coherent Mode (QCM)

The increases of density and its gradient prior to each ELM onset were observed in the pedestal region, which may be caused by an inward particle flux induced by quasi-coherent mode (QCM) ($f = 30\text{--}70$ kHz). The QCM localizes in the pedestal, leads to the increase of density gradient, and has strong nonlinear interaction with the turbulence [12]. Figure 25 shows this physical process. It could be observed that this process could be divided into three phases. Phase 1 in Fig. 25 is characterized by the evolution of the edge pedestal without distinct coherent fluctuation. Phase 2 is denoted by the shaded area with a duration time about 300 ms. In phase 3, the D_α emission increases dramatically. It should be noted that, in phase 2, the coherent fluctuation gradually grows, saturates and starts to decay, and the mode is radially localized with a frequency of 30–70 kHz. The electron density keeps increasing until the end of this phase (Fig. 25b). The decreases abruptly at the end of this phase, while L_{Te}^{-1} increases obviously (Fig. 25c), keeping the L_{pe}^{-1} changing moderately (Fig. 25d). Figure 25e shows that the inward particle flux induced by QCM also increases firstly and then decreases. The observations indicate that a dynamic transition of the

Fig. 23 plasma parameters of a high beta H-mode discharge. **a** NBI heating power from two beams, **b** plasma current, **c** line-averaged electron density, **d** $D\alpha$ signal, **e** plasma stored energy, **f** and **g** normalized beta (β_N)

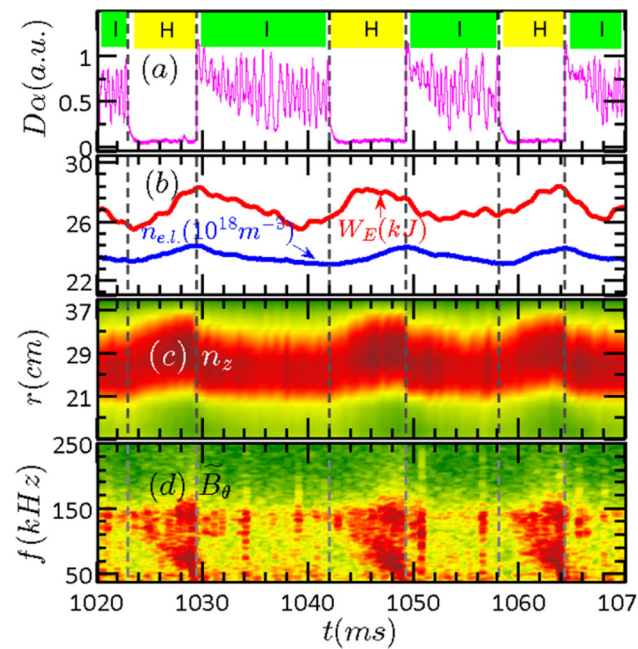
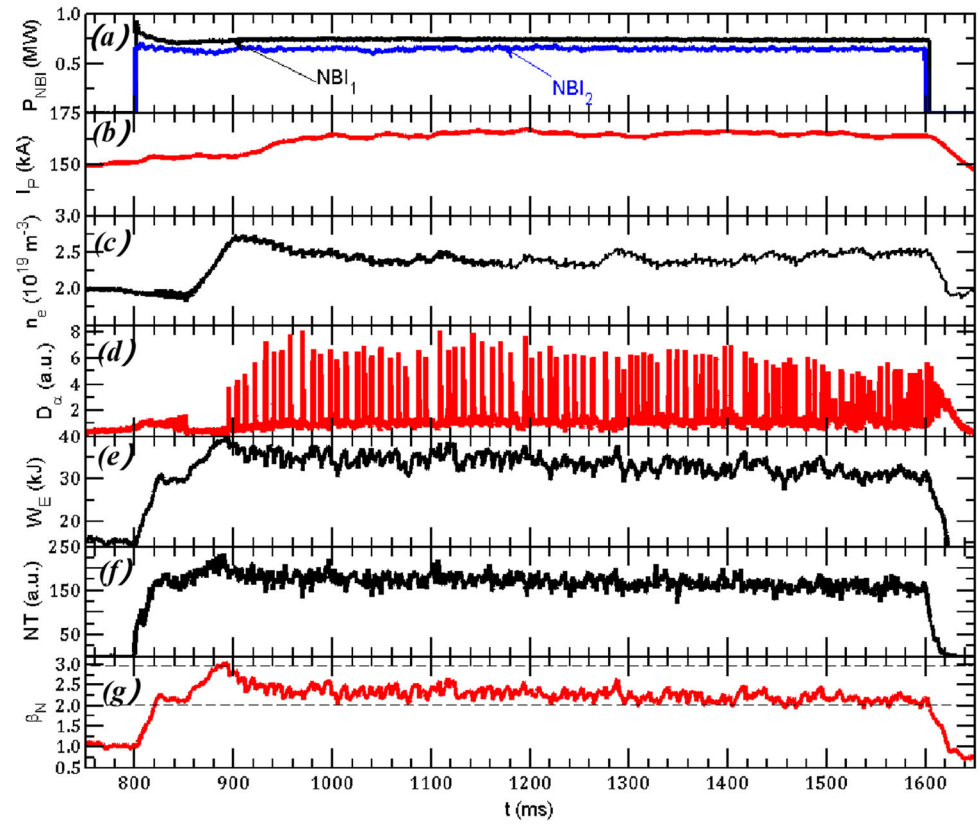


Fig. 24 **a** Divertor D_α signal, **b** inner stored energy and line-averaged I_{bolm}/n_e , with I_{bolm} being the emissivity reconstructed from electron density, **c** effective impurity density and **d** spectrogram of magnetic fluctuations. Reprint from [67], with the permission of APS Publishing

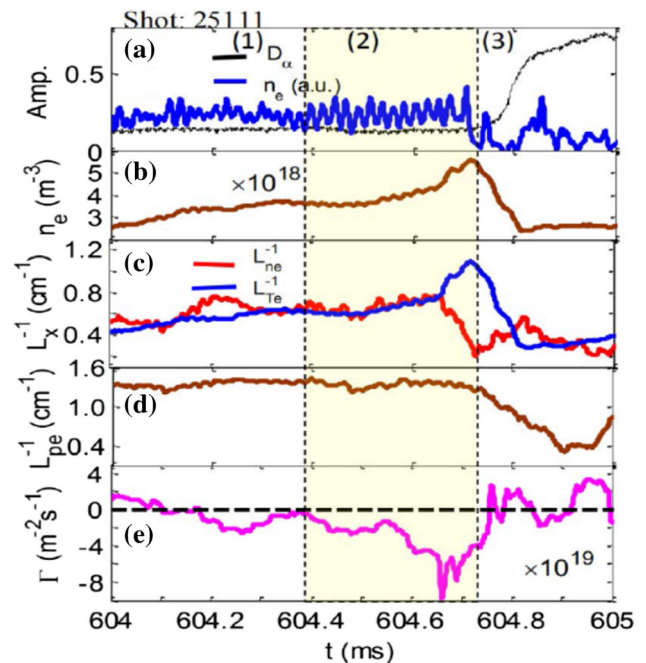


Fig. 25 **a** Temporal evolutions of D_α and the density fluctuation, **b** the pedestal density, **c** the inverses gradient scale lengths of the density and electron temperature, **d** electron pressure, and **e** the particle flux induced by the QCM. Reprint from [12], with the permission of IOP Publishing

plasma exists prior to the ELM onset. Phase 3 is the recovery phase, during which the parameters recover smoothly and connect to phase 1.

From the experimental results, it suggests that the generation of QCM may be related to the nonlinear coupling of small-scale turbulence. More detailed experimental and theoretical investigations are needed to make a conclusion on the instability that affects the pedestal dynamics [68].

Edge Localized Mode Control

During an ELMy H-mode discharge, the strong gradient of plasma edge pressure can trigger repetitive bursts of high transient heat loads on plasma-facing components (PFCs). For the recent decades, since the parameters are significantly improved during the discharges in tokamaks and would be much higher in future reactors, optimal and robust techniques for heat load and ELM control are highly desirable. This section presents the ELM control techniques applied to the HL-2A device.

ELM Control with SMBI

SMBI is one of the effective ELM control techniques applied to the HL-2A tokamak [69]. Then, this technique is developed after the findings that the cooled SMBI could penetrate deeper than the normal SMB into the plasma. The SMBI system modified to form the clusters (similar to micro-pellets) by cooling is developed and used in the ELM control experiments. Then, ELM mitigation experiments with SMBI also performed well in experimental campaigns on EAST [70] and KSTAR [71], and the experimental results from HL-2A are all confirmed. In addition, the results on EAST and KSTAR show that the ELM mitigation with SMBI is more efficient, for example, lasting a longer period time after an SMBI pulse, for type-I ELMy H-mode than for type-III ELMy H-mode, indicating the possibility of application to ELM mitigation on ITER although a more detailed investigation is urgently needed.

ELM Control with LHCD

ELM mitigation with LHCD is achieved in HL-2A when the plasma line-averaged electron density exceeds $2.5 \times 10^{19} \text{ m}^{-3}$ and the absorbed LHCD power is larger than 200 kW [72]. In the HL-2A experiments, no ergodization of magnetic topology and no density pump-out have been observed. The ELM mitigation is synchronized with the pedestal turbulence enhancement, but not with the LHCD pulse [73].

A discharge using LHCD to mitigate ELMs is shown in Fig. 26. The LHCD monitor signal (blue line) and the loop voltage signal (black line) are shown in Fig. 26b. The loop

voltage drop is not visible in the present ELM mitigation experiments, because the plasma density is high, and the number of fast electrons should be strongly reduced due to the thermalization. The ELMs are represented by the spikes in the bolometer signal (Fig. 26c) and also the ion saturated current by divertor Langmuir probes (Fig. 26f). The ELM mitigation is characterized by the ELM frequency increase and its amplitude decrease as shown in Fig. 26b and c, respectively. The radial wavenumber spectrum $S(k_r)$ in Fig. 26d can be obtained from the radial adjacent DBS channels. It could be observed that the wavenumber spectrum shifted to zero direction during mitigation. In Fig. 26h the spectrum before and after mitigation also clearly shows the shift along with the increase of the turbulence amplitude. Figure 26e also presents the time evolution of the pedestal turbulence intensity calculated by integrating the frequency power spectrum with the selected poloidal wavenumber by DBS. It is very clear that the ELM mitigation is desynchronized with the LHCD pulse, but closely correlated to the pedestal turbulence enhancement (Fig. 26e). During ELM mitigation, the pedestal pressure gradient decreases a little after LHCD in Fig. 26g, possibly due to the slight degradation of the plasma confinement [73]. The analysis of the E_r shear rate components shows that the dramatic drop of the ion diamagnetic term, which would be due to the absorption of the high N components of the lower hybrid wave at the plasma edge, would lead to the sharp reduction of $E \times B$ velocity shear rate $\gamma_{E \times B}$ [73]. In addition, a modified turbulence radial wavenumber spectral shift model has been successfully used to simulate the experimental results. Good agreement has been found between experiment and theory for the regulation of the turbulence amplitude with its averaged radial wavenumber [74]. The pedestal turbulence varies before the ELM mitigation phase, which indicates that the ELMs might be mitigated by the enhanced pedestal turbulence through the nonlinear interactions.

ELM Mitigation/Suppression by LBO Impurity Seeding

A laser blow-off (LBO) impurity injection system has been built for HL-2A [25]. This system is installed on the equatorial-plane port and the impurities are vertically injected into the plasma. With this system, different kinds of metal impurities (Al, Fe, W) were separately injected into the ELMy H-mode plasma. The deposition location of the LBO-seeded impurity is observed with a bolometer array and a fast visible camera. ELM mitigation is achieved by LBO-seeded Al and Fe impurity. In addition, ELM suppression is also realized by LBO-seeded Al, Fe and W impurity [75].

Figure 27 shows an ELM mitigation case by the LBO-seeded Fe impurity. Figure 27a is the divertor $D\alpha$ signal

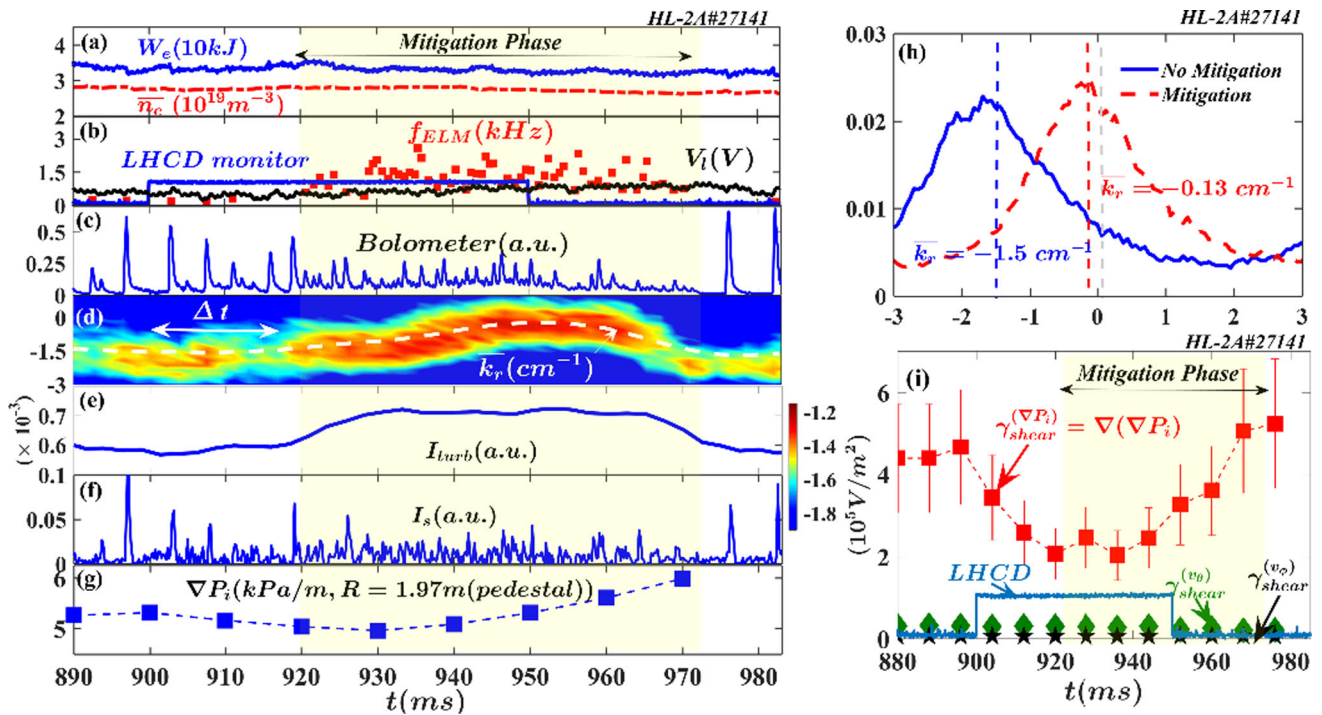


Fig. 26 H-mode discharge triggered by neutral beam heating (1 MW) with ELMs mitigated by LHCD with a significant time delay (plasma current 145 kA, toroidal field 1.3 T, major radius 1.65 m, minor radius 0.4 m). **a** Plasma density (red dashed) and internal stored energy (blue solid); **b** the LHCD monitor signal (blue solid), the loop voltage (black line), and the ELM frequency (red solid square); **c** the bolometer signal; **d** the averaged radial wavenumber; **e** the pedestal

turbulence intensity; **f** ion saturated current from divertor Langmuir probes; **g** ion pressure gradient P_i at pedestal; **h** the radial wavenumber spectra before (blue solid) and during (red dashed) the ELM mitigation; **i** Time evolution of the three components of $E \times B$ velocity shear rate calculated by the data from CXRS. Reprint from [73], with the permission of IOP Publishing

and the ELM mitigation phase is noted by the double arrows. Figure 27b and c show, respectively, the time evolution of the density fluctuation power spectra in the pedestal top and foot, which are measured by the Doppler reflectometry. During the ELM mitigation, the density fluctuations are enhanced obviously. This phenomenon is the same as what has been observed during the ELM mitigation with LHCD. Figure 27d is the plasma radiation power density measured with a bolometer array. From this figure, it can be seen that the clear image of the LBO-seeded impurity in plasma appears at about 903 ms and lasts for about 7 ms. The LBO-seeded impurity particles penetrate the edge plasma and are mainly deposited in the pedestal region. This corresponds to the observation from the fast visible camera.

In addition, ELM suppression has also been obtained in the experiments with LBO-seeded Al, Fe and W impurities. ELM suppression is triggered when the amount of the LBO-seeded impurity exceeds a certain threshold value [75]. The pedestal density fluctuation is significantly reduced during ELM suppression phase, and a harmonic coherent mode is excited, suggesting that HCM could extend the Peeling–Ballooning instability limit.

ELM Control with SMBI Impurity Seeding

Impurity seeding experiments by using SMBI have been performed in ELMy H-mode plasmas. Different from the LBO metal impurity seeding, SMBI seeded the impurity gas into the plasma. In our experiment, the Ne was used. The Ne impurity gas was mixed with main ion fuelling gas D_2 by different ratios (10%, 30% and 100%) and then was seeded into the ELMy H-mode plasmas [76].

It has been observed that the ELM behavior varied with the impurity ratio of the mixture SMBI [76]. The change of the ELM frequency is defined as the ratio of the ELM frequency after the SMBI (f_{ELM}^{after}) to the frequency of the natural ELMs before the SMBI (f_{ELM}^{before}). The value $f_{ELM}^{after}/f_{ELM}^{before}$ is less than 1, meaning the ELM frequency decreases. For 10% Ne mixture SMBI, the ELM frequency ratio is about 2 and ELMs are clearly mitigated. This mitigation effect is similar to that of the main ion fuelling D_2 . For the case of 30% Ne, the ratio of the high frequency bursts (HFBs) frequency after the SMBI to f_{ELM}^{before} reaches to 3.5–5.5. ELMs are replaced by small amplitude HFBs. SMBI with 10% and 30% Ne cases show similar plasma profiles. For the case of 100% Ne (pure Ne), the frequency ratio decreases to 1/2 while the ELM amplitude does not

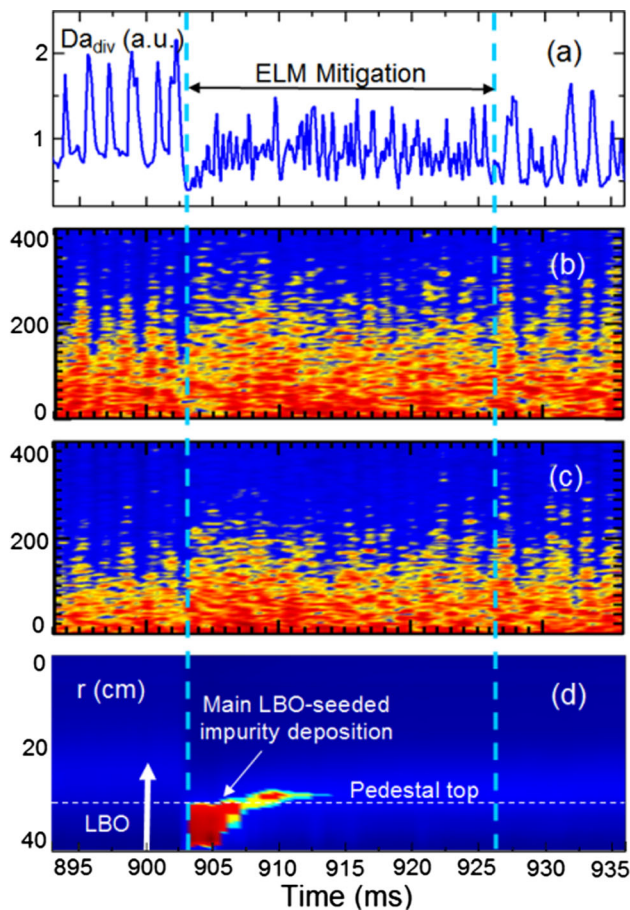


Fig. 27 Observation of the harmonic coherent mode (HCM) during the ELM suppression phase. **a** Divertor D_α signal, **b** Mirnov signal, and **c** time–frequency spectrum of the Mirnov signal. Here, the LBO system was triggered at 900 ms for W impurity injection. Reprint from [75], with the permission of IOP Publishing

double correspondingly, and the ion temperature and electron density at the pedestal region increase indicating the confinement improvement.

Figure 28 shows the 30% Ne mixture SMBI seeding case and the response of the divertor heat flux to the 30% Ne mixture SMBI seeding. In this case, ELMs are suppressed and replaced by HFBs which have a much smaller amplitude compared to ELMs. The impurity mixture seeding is expected to reduce the divertor heat loads. The divertor heat flux is measured by electrostatic probes at the outer divertor plate. The measured location ($z = -830$ mm) is near the striking point. Unfortunately, the profile of the heat flux is not available for these discharges. Compared to the peak heat flux caused by ELMs, the flux of the HFBs is about 10% of the former one as seen from Fig. 28b and c. It indicates that the divertor heat flux is significantly reduced. Also, the pedestal particle transport enhancement has also been observed.

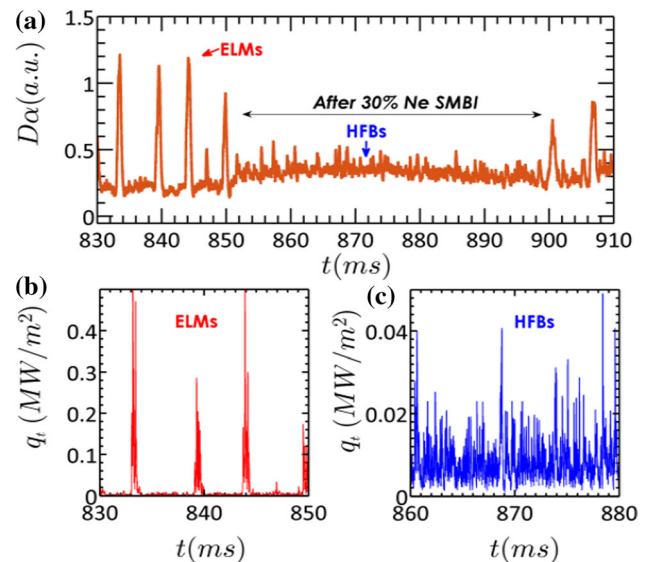


Fig. 28 Response of ELMs and divertor heat flux to 30% Ne mixture SMBI seeding. **a** divertor D_α signal, heat flux at the outer divertor plate ($z = -830$ mm) **b** before and **c** after the SMBI. Reprint from [76], with the permission of IOP Publishing

The result, that ELM activities change with the ratio of the seeded impurity, suggests that there should be an optimal impurity ratio for efficient heat load control in ELMy H-mode plasmas, which would be further investigated in the next step.

ELM Control with RMP

RMP has been experimentally established as an efficient way of controlling ELMs in H-mode tokamak plasmas [77]. On HL-2A, ELM mitigation by RMP was also achieved [78]. The RMP coils are grouped in 2 sets, with each set consisting of two small single turn rectangular coil ($417 \text{ mm} \times 263 \text{ mm}$). They are configured as “+ − +” with $n = 1$ mode dominant. Figure 29 shows a discharge with the ELM mitigation by RMP on HL-2A. In this discharge, the plasma current is about 130kA. The line-averaged density is higher than $2.5 \times 10^{19} \text{ m}^{-3}$, and the pump-out effect on density after the application of RMP is observed. The ELMs are represented by the D_α signal in Fig. 29a. It could be observed that the ELMs are mitigated during RMP. The signal of the RMP coil is shown by the RMP current in Fig. 29b. Figure 29c and d show the heat flux peak and heat flux distribution respectively. The heat flux peak at the divertor decreases due to the mitigation of ELMs by RMP.

MARS-F code was employed to carry out the RMP computation based on the HL-2A experimental configuration. It is found that the edge-peeling response is the main reason leading to the ELM mitigation [79].

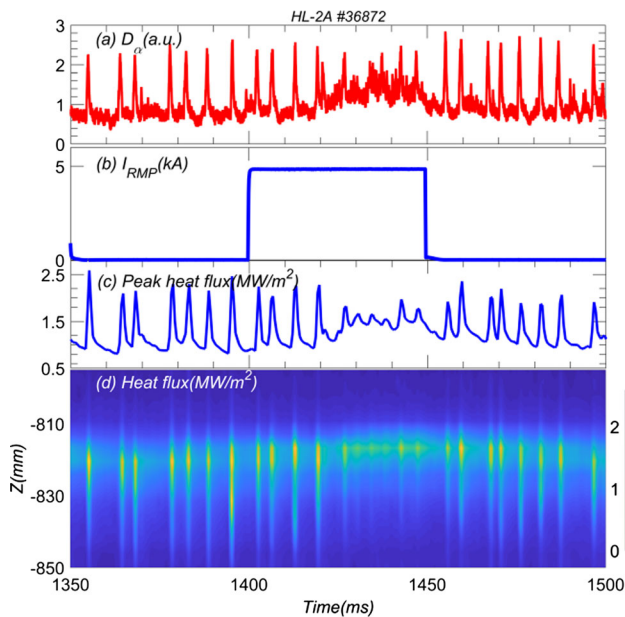


Fig. 29 The time evolutions of **a** the D_α signal, **b** current of the RMP coil, **c** heat flux peak and **d** heat flux distribution

Summary

Over the last several years, the HL-2A research team has achieved significant progress in the areas of lower-hybrid wave heating and current drive, plasma confinement and turbulent transport, MHD instabilities and energetic particle physics and H-mode and ELM control as summarized below:

1. Heating and current drive.

The power coupling of the LHW system on HL-2A during high density H-mode plasma is continuously improved to 1.4 MW. The measurement by the newly installed hard X-ray system shows that the power is mainly deposited at the plasma core. The characteristics of the co-current and counter-current drive have been investigated, which could be achieved by adjusting the wave spectrum. The results show that the LHW system working in co-current drive mode could reach the higher driving efficiency. Full non-inductive LHCD has been achieved in this direction by optimizing the wave spectrum.

2. Confinement and transport.

In the edge plasma of HL-2A tokamak, the turbulent energy concentrates into low frequency area from high frequency region due to inverse energy cascade. This highlights the modulation mechanism in turbulence which is relevant to the generation of GAM zonal flow. The turbulent kinetic energy transferred from intermediate frequencies (20–80 kHz) into ZFs and GAMs enhances as the heating power is increased. Besides, GAMs and magnetic fluctuations can transfer energy through nonlinear

synchronization. The intrinsic poloidal torque characterized by the divergence of the residual stress is deduced from synthesis for the first time in a tokamak plasma. The dynamics of spectral symmetry breaking in drift wave turbulence is in good agreement with the development of the poloidal torque to drive the edge poloidal flow. The influence of the cross-phase dynamics on turbulent stress are investigated. The collapse of the edge shear layer is found to be caused by the decrease of the turbulent drive (Reynolds power) and may lead to edge cooling which is relevant to the density limit. Besides, the turbulence-induced zonal flow and pressure-gradient-induced drift play essential roles in the dynamics of low-intermediate-high-confinement transitions. Blob structures and motions are investigated in the SOL of HL-2A tokamak. The increasing turbulent energy and the spontaneous $E \times B$ flow shear are identified to be responsible for the generation of blobs.

The impurity diffusivity and convection velocity are found to be significantly enhanced in the radial range of $\rho \leq 0.5$ when ECRH is deposited inside the inversion radius of the sawtooth crash. The ion ITBs are firstly observed in NBI heated plasmas at the HL-2A tokamak. The ion thermal transport inside the barrier was reduced to the neoclassical level. The micro-scale turbulence is modulated by the rotation of the macro-scale tearing mode, with a minimum value at the island O-point and maximum at the X-point, consistent with the gradient-driven mechanism of the turbulence. The influence of the magnetic island on turbulence is linked to a critical island width. The interplay between the nonlocal transport and NTM during transient nonlocal heat transport events was observed for the first time. The nonlocal response of the core electron temperature to the edge cooling leads to a locally enhanced pressure gradient at the rational surface and hence the onset of NTM, which in turn, regulates the nonlocal transport by truncation of avalanches.

3. MHD and energetic particle.

Series of MHD instabilities with novel characteristics have been observed on HL-2A. The formation and evolution of quasi-interchange mode is firstly revealed by electron cyclotron emission imaging systems and it will contribute to further understanding of sawtooth oscillations in laboratory and space plasmas. The discoveries of $m/n = 2/1$ fishbone-like mode, non-resonant internal kink modes, energetic particles driven BAEs and AITG mode enrich the knowledge for the wave-particle interaction. Three kinds of axisymmetric modes in BAE, TAE and EAE frequency regions, are driven unstable by nonlinear mode coupling and the nonlinear generation process is well explained by nonlinear gyrokinetic theory. The HL-2A experiments suggest that the fishbone modes can be mitigated and suppressed by electron cyclotron resonance heating,

depending not only on the injected power but also on the radial deposition location of ECRH. Finally, a real-time control system based on ECRH is successfully developed, and it is used to suppress the conventional/neoclassical tearing modes. The new finding and technology will provide technology bases for active control of the energetic particle modes and MHD instability in the future burning plasma.

4. H-mode and ELM control.

The physics during L-I-H has been precisely investigated. The dynamics of the edge plasma flows and turbulence during the L-I-H transition have been investigated by using Doppler reflectometry. It has been observed that GAM exists in L mode and gradually decreases with the generating of LCO during L-I transition. GAM and LCO coexist for a short time and disappear in the H-mode plasma with the increasing of $E \times B$ shear flow before the I-H transition, which takes place in turbulence suppression. In addition, HL-2A has firstly achieved the H-mode discharge with the normalized beta $\beta_N > 3$. In terms of the large size of ELMs, different techniques, such as LHW, ECRH, RMP, and impurity seeding by LBO and SMBI, have been applied to successfully control the large ELMs. It has been found that pedestal turbulence enhancement should be responsible for the observed mitigation effect.

These achievements in HL-2A plasmas will definitely deepen our understanding on the key physical topics relevant to ITER and advanced tokamak operation, such as the HL-2M operation. The next experimental campaign of HL-2A will promote the following research aspects: high performance plasma operation, development of advanced ELM control techniques, multi-scale interactions between MHD, EP mode and turbulence, core–edge coupling physics, and the control of NTM, EP modes as well as plasma disruption.

Acknowledgements The authors would like to thank all colleagues who have contributed to the HL-2A projects in the aspect of diagnostic developments and physics studies. This work is supported by the Nuclear Power Development Research Project under Grant No. H6600003-17.

References

- X.R. Duan et al., Nucl. Fusion **49**, B87 (2009)
- L.W. Yan et al., Rev. Sci. Instrum. **88**, 113504 (2017)
- R. Ke, Y.F. Wu, G.R. McKee et al., Rev. Sci. Instrum. **89**(10), 10D122 (2018)
- S. Gong, Y. Yu, M. Xu et al., Plasma Sci. Technol **21**(8), 084001 (2019)
- K.R. Fang et al., Rev. Sci. Instrum. **90**, 063503 (2019)
- B.D. Yuan, Y. Yu, R.C. He et al., Rev. Sci. Instrum. **91**(7), 073505 (2020)
- T. Long et al., Rev. Sci. Instrum. **91**(8), 083504 (2020)
- X.R. Duan et al., Nucl. Fusion **57**, 102013 (2017)
- Y.P. Zhang et al., AIP Adv. **9**, 085019 (2019)
- B. Lu et al., RFPPC2019, May 14–17, 2019, Hefei China. I2–06
- Y. Peysson et al., Plasma Phys. Control. Fusion **42**, B87 (2000)
- M. Xu et al., Nucl. Fusion **59**, 112017 (2019)
- Y. Shen, J.Q. Dong, Z.B. Shi et al., Nucl. Fusion **59**(4), 044001 (2019)
- M. Xu, G.R. Tynan, P.H. Diamond et al., Phys. Rev. Lett. **108**(24), 245001 (2012)
- G.R. Tynan, M. Xu, P.H. Diamond et al., Nucl. Fusion **53**(7), 073053 (2013)
- K.J. Zhao, Y. Nagashima, P.H. Diamond et al., Phys. Rev. Lett. **117**(14), 145002 (2016)
- T. Long, P.H. Diamond, M. Xu et al., Nucl. Fusion **59**(10), 106010 (2019)
- Z.B. Guo, P.H. Diamond, Phys. Rev. Lett. **114**(14), 145002 (2015)
- D. Guo, L. Nie, R. Ke et al., Nucl. Fusion **58**(2), 026015 (2018)
- R. Hong, G.R. Tynan, P.H. Diamond et al., Nucl. Fusion **58**(1), 016041 (2018)
- J. Cheng, J.Q. Dong, K. Itoh et al., Phys. Rev. Lett. **110**(26), 265002 (2013)
- B. Yuan, M. Xu, Y. Yu, J. Instrum. **13**(03), C03033 (2018)
- J. Yuan, B. Yuan, M. Xu et al., Plasma Sci. Technol. **21**(8), 084002 (2019)
- J. Cheng, J.Q. Dong, L.W. Yan et al., Nucl. Fusion **53**(9), 093008 (2013)
- Z.Y. Cui et al., Nucl. Fusion **53**, 093001 (2013)
- Z.Y. Cui et al., Nucl. Fusion **58**, 056012 (2018)
- R. Dux, STRAHL user manual Technical Report No. 10/30 IPP Garching Germany (2006). http://pubman.mpdl.mpg.de/pubman/item/escidoc:2143869/component/escidoc:2143868/IPP_10_30.pdf. Accessed 30 Oct 2006
- D.L. Yu et al., Nucl. Fusion **56**, 056003 (2016)
- L. Bardóczi et al., Phys. Rev. Lett. **116**, 215001 (2016)
- W. Chen et al., Nucl. Fusion **57**, 114003 (2017)
- M. Jiang et al., Rev. Sci. Instrum. **84**, 113501 (2013)
- Z.B. Shi et al., Rev. Sci. Instrum. **87**, 113501 (2016)
- M. Jiang et al., Nucl. Fusion **58**, 026002 (2018)
- A.B. Navarro et al., Plasma Phys. Control. Fusion **59**, 034004 (2017)
- M. Jiang et al., Nucl. Fusion **59**, 066019 (2019)
- R. Fitzpatrick, Phys. Plasmas **2**, 825 (1995)
- O. Pan et al., Nucl. Fusion **55**, 113010 (2015)
- W. Chen et al., Nucl. Fusion **56**, 044001 (2016)
- X.Q. Ji et al., Sci. Rep. **6**, 32697 (2016)
- P.W. Shi et al., Phys. Plasma **25**, 062506 (2018)
- W. Chen et al., Nucl. Fusion **59**, 096037 (2019)
- X.L. Zhu et al., Nucl. Fusion **60**, 046023 (2020)
- L.M. Yu et al., Nucl. Fusion **57**, 036023 (2017)
- L.M. Yu et al., Nucl. Fusion **53**, 053002 (2013)
- W. Chen et al., Nucl. Fusion **50**, 084008 (2010)
- G. Meng et al., Phys. Plasma **22**, 092510 (2015)
- P.W. Shi et al., Nucl. Fusion **59**, 066015 (2019)
- F. Zonca et al., Plasma Phys. Control. Fusion **38**, 2011–2028 (1996)
- W. Chen et al., Nucl. Fusion **56**, 036018 (2016)
- W. Chen et al., Nucl. Fusion **58**, 056004 (2018)
- L. Chen, F. Zonca, Phys. Plasma **20**, 055402 (2013)
- P.W. Shi et al., Nucl. Fusion **59**, 086001 (2019)
- Z. Chang et al., Nucl. Fusion **35**, 1469 (1995)
- K.G. McClements et al., Nucl. Fusion **42**, 1155 (2002)
- W. Chen et al., Europhys Lett. **107**, 25001 (2014)
- Y.P. Zhang et al., Nucl. Fusion **55**, 113024 (2015)
- P.W. Shi et al., Nucl. Fusion **60**, 064001 (2020)
- K. Nagaoka et al., Nucl. Fusion **53**, 072004 (2013)
- S. Yamamoto et al., Nucl. Fusion **57**, 126065 (2017)

60. W. Chen et al., Nucl. Fusion **58**, 014001 (2018)
 61. H. Zohm, Plasma Phys. Control. Fusion **38**, 105 (1996)
 62. A.S. Liang et al., Phys. Plasmas **25**, 022501 (2018)
 63. A.S. Liang et al., Nucl. Fusion **60**, 092002 (2020)
 64. P. Sauter et al., Nucl. Fusion **52**, 012001 (2012)
 65. C.F. Maggi et al., Nucl. Fusion **54**, 023007 (2014)
 66. W.L. Zhong et al., Nucl. Fusion **60**, 082002 (2020)
 67. W.L. Zhong et al., Phys. Rev. Lett. **117**, 045001 (2016)
 68. J. Cheng et al. Preprint: 2018 IAEA Fusion Energy Conf. (Gandhinagar, India, 22–27 October) EX/P5-6 (2018)
 69. W.W. Xiao et al., Nucl. Fusion **52**, 114027 (2012)
 70. X. L. Zou, et al. Proc. 24th Fusion Energy Conf. (San Diego, CA, 2012) (Vienna: IAEA) PD/P8–08 (2012). www.naweb.iaea.org/naweb/physics/FEC/FEC2012/html/fec12.htm. Accessed 12 Oct 2012
 71. W.W. Xiao et al., Nucl. Fusion **54**, 023003 (2014)
 72. G.L. Xiao et al., Phys. Plasmas **24**, 122507 (2017)
 73. G.L. Xiao et al., Nucl. Fusion **59**, 126033 (2019)
 74. G.L. Xiao et al., Phys. Plasmas **26**, 072303 (2019)
 75. Y.P. Zhang et al., Nucl. Fusion **58**, 046018 (2018)
 76. W.L. Zhong et al., Nucl. Fusion **59**, 076033 (2019)
 77. T.F. Sun et al., Fusion Eng. Des. **148**, 111301 (2019)
 78. T.F. Sun et al., Nucl. Fusion (2021). <https://doi.org/10.1088/1741-4326/abd2c7>
 79. Y.Q. Liu et al., Plasma Phys. Control. Fusion **58**, 114005 (2016)
- Publisher's Note** Springer Nature remains neutral with regard to jurisdictional claims in published maps and institutional affiliations.